Geochemistry Geophysics Geosystems G3
AN ELECTRONIC JOURNAL OF THE EARTH SCIENCES
Published by AGU and the Geochemical Society

Article
Volume 9, Number 5
15 May 2008
Q05008, doi:10.1029/2007GC001834
ISSN: 1525-2027

Integrated geophysical-petrological modeling of the lithosphere and sublithospheric upper mantle: Methodology and applications

J. C. Afonso and M. Fernàndez
Group Dynamics of the Lithosphere, Institute of Earth Sciences "J. Almera", CSIC, Luís Solé i Sabarís s/n, E-08028 Barcelona, Spain (jafonso@ija.csic.es; mfernandez@ija.csic.es)

G. Ranalli
Department of Earth Sciences and Ottawa-Carleton Geoscience Centre, Carleton University, 1125 Colonel By Drive, Ottawa, Canada K1S 5B6 (granalli@earthsci.carleton.ca)

W. L. Griffin
GEMOC ARC Key Centre for Geochemical Evolution and Metallogeny of Continents, Department of Earth and Planetary Sciences, Macquarie University, Sydney, NSW 2109, Australia (wgriffin@els.mq.edu.au)

J. A. D. Connolly
Earth Sciences Department, Swiss Federal Institute of Technology, Soneggstr. 5, CH-8092 Zurich, Switzerland (james.connolly@erdw.ethz.ch)

[1] A combined geophysical-petrological methodology to study the thermal, compositional, density, and seismological structure of lithospheric/sublithospheric domains is presented. A new finite-element code (LitMod) is used to produce 2-D forward models from the surface to the 410-km discontinuity. The code combines data from petrology, mineral physics, and geophysical observables within a self-consistent framework. The final result is a lithospheric/sublithospheric model that simultaneously fits all geophysical observables and consequently reduces the uncertainties associated with the modeling of these observables alone or in pairs, as is commonly done. The method is illustrated by applying it to both oceanic and continental domains. We show that anelastic attenuation and uncertainties in seismic data make it unfeasible to identify compositional variations in the lithospheric mantle from seismic studies only. In the case of oceanic lithosphere, plates with thermal thicknesses of 105 ± 5 km satisfy geophysical and petrological constraints. We find that Vp are more sensitive to phase transitions than Vs, particularly in the case of the spinel-garnet transition. A low-velocity zone with absolute velocities and gradients comparable to those observed below ocean basins is an invariable output of our oceanic models, even when no melt effects are included. In the case of the Archean subcontinental lithospheric mantle, we show that "typical" depleted compositions (and their spatial distribution) previously thought to be representative of these mantle sections are compatible neither with geophysical nor with petrological data. A cratonic keel model consisting of (1) strongly depleted material (i.e., dunitic/harzburgitic) in the first 100–160 km depth and (2) less depleted (approximately isopycnic) lower section extending down to 220–300 km depth is necessary to satisfy elevation, geoid, SHF, seismic velocities, and petrological constraints. This highly depleted (viscous) upper layer, and its chemical isolation, may play a key role in the longevity and stability of cratons.

Components: 20,624 words, 15 figures, 3 tables.

Keywords: oceanic lithosphere; Archean lithosphere; modeling; seismic attenuation; xenoliths; mantle composition.

Index Terms: 8124 Tectonophysics: Earth's interior: composition and state (1212, 7207, 7208, 8105); 7218 Seismology: Lithosphere (1236); 3621 Mineralogy and Petrology: Mantle processes (1038).

Received 24 September 2007; **Revised** 19 February 2008; **Accepted** 24 March 2008; **Published** 15 May 2008.

Afonso, J. C., M. Fernàndez, G. Ranalli, W. L. Griffin, and J. A. D. Connolly (2008), Integrated geophysical-petrological modeling of the lithosphere and sublithospheric upper mantle: Methodology and applications, *Geochem. Geophys. Geosyst.*, *9*, Q05008, doi:10.1029/2007GC001834.

1. Introduction

[2] The determination of the lithosphere's thermal and compositional structure in space and time is one of the fundamental goals in modern lithospheric modeling. It provides crucial information not only for interpreting present-day lithospheric features, but also on how the lithospheric-sublithospheric system would respond to perturbations arising from tectonic shortening, rifting and sublithospheric convection. In this context, much of the current knowledge about the present-day thermal and compositional structure of the lithospheric and sublithospheric upper mantle comes essentially from three independent modeling approaches. The most widely used methodology makes use of geophysical observables such as gravity, surface heat flow (SHF), elevation, or some combination of these, as constraints to the model [e.g., *Lachenbruch and Morgan*, 1990; *Zeyen and Fernàndez*, 1994; *Zeyen et al.*, 2005; *Ebbing et al.*, 2006; *Fullea et al.*, 2007]. These methods are based on concepts of thermal and/or isostatic equilibrium where the density of the lithospheric mantle is either taken as constant or only temperature dependent. The density of the sublithospheric mantle is assumed to be constant everywhere, and its composition identical to that of its lithospheric counterpart. Although this method has been proven to be a fair first-order approximation, the neglect of compressibility, phase changes, and compositional heterogeneities within the upper mantle leads to inconsistencies when comparing the resulting mantle density with tomography, xenolith, and thermodynamic data. It also creates artificial density contrasts at the top (Moho) and bottom (the so-called lithosphere-asthenosphere boundary or LAB) of the lithosphere that can affect the modeling and interpretation of gravity and geoid anomalies.

[3] The second approach to study the thermal and/or compositional structure of the lithospheric-sublithospheric upper mantle is based on seismic data. This method relies upon an appropriate combination of "observed" seismic velocities (usually shear waves) with mineral physics, laboratory data, and thermodynamic concepts [e.g., *Ritzwoller et al.*, 2004; *Deen et al.*, 2006; *Priestley and McKenzie*, 2006]; the key factor is the assumed or derived functional relationship used to convert velocities into either thermal and/or compositional heterogeneities. Although this approach certainly provides a unique direct probe of mantle structure, it is far from being free of ambiguities. The possibility of distinguishing compositional from thermal effects using only seismic information is still unclear [e.g., *Cammarano et al.*, 2003; *Lee*, 2003; *Artemieva et al.*, 2004; *Afonso et al.*, 2005; *Faul and Jackson*, 2005; *Deen et al.*, 2006; *Priestley and McKenzie*, 2006; *Schutt and Lesher*, 2006]. Uncertainties associated with low spatial resolution, anisotropy, composition variability, grain-size dependence, anelasticity, and geotherm estimations further complicate the task. Even when using similar velocity data, the different parameterizations used by different authors result in significant discrepancies between models (see, e.g., differences of >100 km in the thermal thickness of North America and Africa as given by *Deen et al.* [2006] and *Priestley and McKenzie* [2006]).

[4] A third source of independent information, but not necessarily representative of present-day conditions, is the petrological-geochemical approach. In this case, thermobarometry and chemical-isotopic analyses in xenoliths and xenocrysts brought up to the surface by volcanic events can be used to estimate the compositional and thermal structure of specific localities at the time of the eruption. *Griffin et al.* [1999b], for instance, have shown that the LAB in continental regions can be defined

as the maximum depth from which low-Y (<10 ppm) garnets, characteristic of depleted lithosphere, are derived. Using thermobarometric techniques, these authors have estimated that the geochemical LAB coincides with temperatures of 1250–1300°C, establishing a close correlation with the thermal definition of the lithosphere (i.e., here understood as the depth of the 1330°C isotherm). Unfortunately, direct observation of the lithospheric-sublithospheric upper mantle is limited to only a few specific tectonic environments (e.g., ophiolites and Alpine peridotites in orogenic belts, xenolith suites in continental volcanic areas, abyssal peridotites in oceanic fracture zones) from which a picture of mantle composition can be obtained at local scale rather than at lithospheric scale. As a result, the large-scale temporal and spatial extrapolations of compositions and thermophysical properties needed when modeling large sections of the Earth carry implicitly unquantifiable uncertainties.

[5] It is clear that if the assumptions behind all these methods were correct, any modeled section of upper mantle should produce consistent results (as long as a consistent database of thermophysical parameters is used), no matter which methodology is applied. Yet, large discrepancies between predictions from these methods are rather common in the literature (see references above). One way to overcome these difficulties and obtain more consistent and robust models, is to fit simultaneously and self-consistently all the available geophysical and petrological observables (i.e., gravity anomalies, geoid height, SHF, electrical conductivity, seismic velocities, xenolith data, and elevation). A simultaneous fit of all these observables reduces the uncertainties associated with the modeling of each of them alone, or with the combinations of pairs commonly used in the literature (see above). It also allows us to distinguish, and have a better control on, thermal or compositional density variations at different depths, since these observables are differentially sensitive to shallow/deep, thermal/compositional density anomalies. However, to our knowledge, an integrated modeling approach that includes all of the above in a self-consistent manner has not been developed so far.

[6] This paper attempts to fill this gap by presenting and applying an integrated geophysical-petrological methodology to study the thermal, compositional, density, and seismological structure of any lithospheric/sublithospheric domain within the upper mantle. The following sections introduce a brief and updated review of the compositional heterogeneities within the lithospheric mantle that affect geophysical modeling (section 2), the physical/mathematical concepts behind our approach (section 3), and the application of it to both oceanic and continental domains (sections 4 and 5). In the case of the oceanic lithosphere, we focus primarily on its thermal and seismological structures, and their implications for the interpretation of tomographic studies, compositional models, and the nature of phase changes. When dealing with the continental lithosphere, we focus the assessment on possible keel models for the Archean subcontinental lithospheric mantle that are compatible with recent compositional estimations and available geophysical evidence. We also show that the identification of compositional variations in the lithospheric mantle from seismic studies only is unreliable.

2. Compositional Heterogeneities in the Lithospheric Mantle

[7] The oceanic lithosphere is generated by partial melting of the convecting mantle at mid-ocean ridges (MORs), to produce a depleted residual mantle and a basaltic crust. Although lateral compositional heterogeneities exist within oceanic lithosphere [e.g., *Michael and Bonatti*, 1985], its vertical stratification in composition (produced at MORs) is dominant. On a large scale it therefore is realistic, for the purposes of geophysical-petrological modeling, to treat the oceanic lithosphere as a vertically stratified plate (see also section 4 and Appendix A) [*Afonso et al.*, 2007]. In contrast, the continental crust and underlying subcontinental lithospheric mantle (SCLM) are highly heterogeneous. The latter ranges in thickness from a few tens of kilometers beneath rift zones, to >250 km beneath some Archean cratons. The SCLM consists mainly of ultramafic rocks, ranging from refractory dunites and harzburgites to lherzolites. This compositional range is commonly represented and interpreted in terms of depletion in basaltic components through partial melting processes. Maximum Re-Os melt-depletion ages for mantle-derived peridotite xenoliths commonly correspond to the oldest radiometric ages of rocks from the overlying crust, particularly in cratonic areas [e.g., *Pearson et al.*, 2002; *Shirey et al.*, 2002; *Griffin et al.*, 2002, and references therein]. In the Siberian Craton, for example, compositionally distinct mantle domains coincide with mapped crustal terranes, indicating that during the assembly of the craton, each terrane carried its own lithospheric root [*Griffin*

Table 1. Estimates of Mean SCLM Compositions From Xenolith Suites and Peridotite Massifs

Archons[a]	Aver. Archon Gnt. SCLM	Aver. Kaapvaal Low-T Lherzolite	Aver. Kaapvaal Harzburg.	Aver. Slave Xenoliths	Aver. Kaapvaal High-T Lherzolite	W. Norway Average Dunite/ Harzburg.	E. Greenland Ave. Xenoliths	Archon "Pristine" Estimate
SiO_2	45.7	46.5	45.9	42.9	44.4	42.9	43.0	42.7
TiO_2	0.04	0.05	0.05	0.00	0.17	0.01	0.00	0.01
Al_2O_3	0.99	1.40	1.3	1.10	1.75	0.21	0.45	0.40
Cr_2O_3	0.28	0.34	0.34	0.50	0.30	0.32	0.43	0.34
FeO	6.4	6.6	6.0	7.2	8.1	6.5	6.5	6.5
MnO	0.11	0.10	0.10	0.10	0.12	0.11	0.18	0.15
MgO	45.5	43.8	45.5	47.2	43.4	49.4	49.0	49.3
CaO	0.59	0.86	0.5	0.60	1.27	0.20	0.12	0.20
Na_2O	0.07	0.10	0.07	0.12	0.12	0.01	0.03	0.10
NiO	0.30	0.29	0.28	0.31	0.26	0.34	0.34	0.30
Mg#	92.7	92.2	93.1	92.1	90.5	93.1	93.1	93.1
Cr/(Cr+Al)	0.16	0.14	0.27	0.10	0.10	0.28	0.17	0.16

Protons[a]	Aver. Proton Gnt. SCLM	Aver. Proton Xenoliths	Aver. Proterozoic Massif	Proton SCLM (Preferred)
SiO_2	44.7	43.9	45.2	44.6
TiO_2	0.09	0.04	0.09	0.07
Al_2O_3	2.1	1.6	2.0	1.9
Cr_2O_3	0.42	0.40	0.38	0.40
FeO	7.9	7.9	7.9	7.9
MnO	0.13	0.12	0.11	0.12
MgO	42.4	43.9	41.6	42.6
CaO	1.9	1.3	1.9	1.7
Na_2O	0.15	0.08	0.13	0.12
NiO	0.29	0.22	0.28	0.26
Mg#	90.6	90.8	90.4	90.6
Cr/(Cr+Al)	0.12	0.15	0.11	0.12

Tectons[a]	Aver. Tecton Gnt. SCLM	Aver. Tecton Gnt. Peridotite	Aver. Spinel Peridotite	Aver. Tecton Peridotite	PUM MS[b]	PUM J79[c]
SiO_2	44.5	45.0	44.0	44.4	45.0	45.2
TiO_2	0.14	0.16	0.09	0.09	0.20	0.22
Al_2O_3	3.5	3.9	2.3	2.6	4.5	4.0
Cr_2O_3	0.40	0.41	0.39	0.40	0.38	0.46
FeO	8.0	8.1	8.4	8.2	8.1	7.8
MnO	0.13	0.07	0.14	0.13	0.14	0.13
MgO	39.8	38.7	41.4	41.1	37.8	38.3
CaO	3.1	3.2	2.2	2.5	3.6	3.5
Na_2O	0.24	0.28	0.24	0.18	0.36	0.33
NiO	0.26	0.24	0.26	0.27	0.25	0.27
Mg#	89.9	89.5	89.8	89.9	89.3	89.7
Cr/(Cr+Al)	0.07	0.07	0.10	0.09	0.05	0.07

[a] Classifications according to *Griffin et al.* [1999b].
[b] PUM composition of *McDonough and Sun* [1995].
[c] PUM composition of *Jagoutz et al.* [1979].

et al., 1999c]. These observations require long-term linkage between the crust and the SCLM.

[8] Studies of xenoliths and xenocrysts in volcanic rocks, and exposed massifs in mobile belts, have shown that the mean composition of the SCLM is broadly related to the tectonothermal age of the overlying crust, defined as the age of the last major thermal event [*Griffin et al.*, 1998, 1999b] (Table 1). Estimates based on the average composition of xenolith suites are subject to bias in sampling, by

both volcanoes and geologists (see section 5), and extensive xenolith suites are few, especially in cratonic areas. However, most kimberlites, and many other types of volcanic rocks, carry garnet xenocrysts derived from disaggregated mantle wall-rocks. *Griffin et al.* [1999b] showed that the compositions of garnets in mantle-derived peridotites are closely linked to whole-rock composition, and derived a series of algorithms that allow the calculation of a bulk composition for any given garnet xenocryst. Mean compositions of SCLM sections calculated from garnet xenocrysts correspond well to mean compositions of xenolith suites [*Griffin et al.*, 1999b]. The application of this technique provides a larger body of data, and hopefully more representative estimates of the composition of the garnet-bearing part of the SCLM.

[9] Archean cratons, with tectonothermal ages >2.5 Ga, generally have highly depleted SCLM, while most SCLM beneath Phanerozoic mobile belts is only mildly depleted relative to estimates of the Primitive Upper Mantle (PUM). SCLM beneath Proterozoic shields and mobile belts, with tectonothermal ages of 2.5–1.0 Ga, typically is intermediate in composition. These compositional variations within the lithospheric mantle are directly reflected in its thermophysical properties (i.e., density, elastic parameters, etc.). For instance, more depleted rocks in the lherzolite-harzburgite spectrum have lower density than less depleted ones. The relatively fertile SCLM typical of Phanerozoic mobile belts is buoyant relative to the underlying asthenosphere when its geotherm is elevated, but will lose this buoyancy on cooling; it will tend to delaminate, with major tectonic consequences [e.g., *Poudjom-Djomani et al.*, 2001; *Zheng et al.*, 2006]. In contrast, Archean SCLM is buoyant relative to the sublithospheric mantle even on the lowest known geotherms, and also is highly refractory and mechanically strong. It therefore is unlikely to delaminate, or to melt extensively, but may suffer repeated episodes of metasomatic refertilization through time. These metasomatic processes, and the tendency for old depleted SCLM to persist, also produce vertical compositional gradients within the SCLM. The SCLM beneath Archean cratons typically becomes more "fertile" with depth, and is bounded by a 10–20 km zone of intense melt-related metasomatism [*O'Reilly and Griffin*, 2006, and references therein]. This may represent a "lithosphere-asthenosphere boundary", but is more likely to reflect the accumulation of rising melts; inasmuch as few xenoliths are derived from below this zone, we have little direct evidence for the composition of the underlying mantle.

[10] It follows from the above discussion that the present-day major-element composition of the lithospheric mantle, and therefore its thermophysical properties, can vary substantially both vertically and horizontally. Hence, any attempt to constraint the thermal (and compositional) structure of the lithospheric-sublithospheric upper mantle should be consistent with these observations.

3. Methodology and Numerical Code

[11] The methodology presented in this paper has been incorporated into a 2-D finite-element code referred to as LitMod (Lithospheric Modeling); a full 3-D version is currently under development. LitMod is a collection of FORTRAN subroutines based on the architecture of the previous finite-element code CAGES [*Zeyen and Fernàndez*, 1994]. The general approach used by CAGES to calculate the thermal structure, SHF, and gravity/geoid anomalies is kept in LitMod with some modifications (see below). However, the methods to estimate elevation, seismic velocities, density structure, and temperature-pressure-composition-dependent parameters are all new or significantly modified. The general modeling procedure, including the necessary input and output files, is summarized in Figure 1.

[12] LitMod divides the numerical domain into triangular elements that make up the different crustal and mantle bodies. The mesh is automatically adjusted to fit the geometry assigned to these bodies, each of which typically represents only one type of lithology and is characterized by its own set of thermophysical parameters (e.g., thermal conductivity, volumetric heat production rate, coefficient of thermal expansion, etc.). The volumetric heat production rate can either be a constant for each body (preferred, since it is mainly a function of lithology [e.g., *Kukkonen and Lahtinen*, 2001]) or an exponential (decreasing) function of depth [cf. *Turcotte and Schubert*, 1982]. The relative effects of temperature and pressure on the density of crustal bodies are taken into account through their respective temperature-pressure-dependent coefficients of thermal expansion (CTE) and compressibilities (β). In the case of the mantle, the full set of equations of state (EoS) for each material is solved

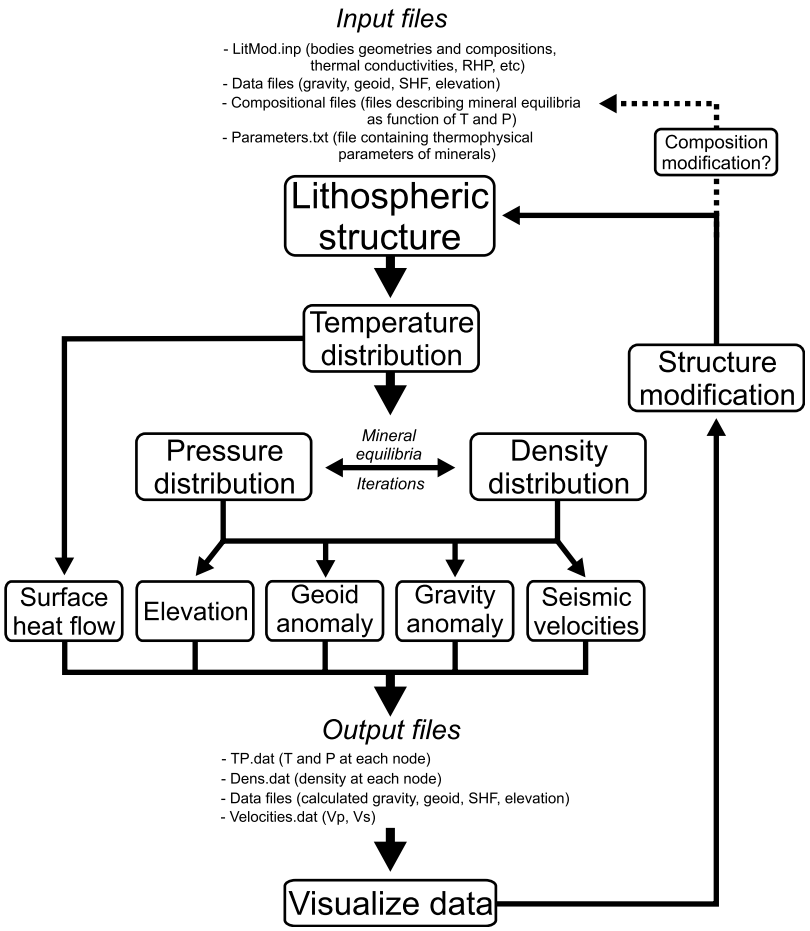

Figure 1. Simplified flowchart indicating the general modeling procedure used in LitMod. Additional output files (listing specific properties) can be obtained if necessary. Pressure and density at each mantle node are obtained through iterations that involve solving for the stable mineral assemblage in each iteration. See text for details.

(see section 3.2). Once a particular structure is defined, the code solves the following algorithms.

3.1. Thermal Modeling and Boundary Conditions

3.1.1. Temperature in the Lithosphere

[13] In the absence of convection/advection, the 2-D steady-state temperature distribution within the lithosphere is described by the familiar conductive heat transfer equation

$$\nabla \cdot (-k \nabla T) - A(x,z) = 0 \qquad (1)$$

where T is temperature, k the thermal conductivity [W m^{-1} K^{-1}], A the volumetric heat production rate [W m^{-3}], and x, z, the horizontal and vertical Cartesian coordinates. For the temperature and pressure dependence of k in the mantle, Hofmeister's model [*Hofmeister*, 1999] is assumed, which gives the relation

$$k_{(T,P)} = k^{\circ}\left(\frac{298}{T}\right)^{a} \exp\left[-(4\gamma + 1/3)\int_{298}^{T} \alpha(T)dt\right] \times \left(1 + \frac{K_0' P}{K_T}\right) + k_{rad}(T) \qquad (2)$$

where k° is the thermal conductivity at $T = 298$ K and $P = 1$ atm (=5.3 W m^{-1} K^{-1}), a is a fitting parameter (=0.45), γ is the thermal Grüneisen parameter (=1.25), $\alpha(T)$ is the T-dependent CTE, K_T is a representative isothermal bulk modulus, $K_0' = dK_T/dP$, and $k_{rad}(T)$ is a function describing the radiative contribution to k (taken from *Hofmeister* [1999, equation (12)]). Strictly, k also varies with composition due to changes in thermodynamic parameters, chemistry, and relative proportions of the constitutive minerals. However, since uncer-

tainties associated with these effects are still large, we choose not to model k as an explicit function of composition.

[14] Equation (1) is solved with the finite-element technique using the Galerkin's ponderation method [e.g., *Zienkiewicz*, 1977], subject to the following boundary conditions: (1) fixed (prescribed) temperature at the surface of the model; (2) no heat flow across the lateral boundaries of the model; and (3) fixed (prescribed) temperature at the bottom of the model. Generally, the choice of the surface temperature, $T_\circ$, is straightforward. Changes of the order of 20°C in $T_\circ$ do not affect the results significantly. The second boundary condition is widely used in thermal modeling and requires no further clarification. The third boundary condition, however, is not always obvious and needs some explanation.

[15] In mantle-like fluids with strongly temperature-dependent viscosity the heat-transfer mechanism changes with depth from conduction-dominated to convection-dominated [*Schubert et al.*, 2001]. Below the rigid stagnant upper part (i.e., lithosphere) there is a rheologically active thermal boundary layer where heat is transferred by both conduction and convection. Numerical simulations indicate that this rheological boundary layer is ~50 km thick, and that the temperature at its base is ~1350–1400°C [*Zaranek and Parmentier*, 2004; *McKenzie et al.*, 2005; S. Zlotnik et al., Small-scale gravitational instabilities under the oceans: Implications for the evolution of the oceanic lithosphere and its expression in geophysical observables, submitted to *Philosophical Magazine*, 2008]. Accordingly, we take the 1330°C isotherm to define the base of the rigid and conductive layer. The region beneath this layer convects vigorously and can be considered approximately adiabatic [e.g., *Schubert et al.*, 2001].

3.1.2. Temperature in the Sublithospheric Mantle

[16] The assumed temperature at the bottom of the model will depend on the model's total thickness. Since our goal is not only the modeling of the lithosphere, but also of the sublithospheric domain approximately down to the 410-km discontinuity, typical pyroxene thermobarometry on peridotite xenoliths is not of much help. Instead, estimations from high-pressure and high-temperature experiments on mineral phase equilibria need to be used [e.g., *Ito and Katsura*, 1989; *Fei and Berkta*, 1999; *Frost*, 2003; *Katsura et al.*, 2004]. The studies by *Ito and Katsura* [1989] and *Katsura et al.* [2004] are of particular relevance here, since they give temperature estimations at 350 and 410 km, respectively, based on phase equilibria of olivine-wadsleyite in the system $(Mg, Fe)_2SiO_4$. By comparing the seismically observed depth of the transition with experimental phase relations, *Katsura et al.* [2004] estimated a temperature of 1487 ± 45°C at the 410-km discontinuity. Taking into account the combined effects of (1) the latent heat released by the phase transformation, (2) the thermal relaxation due to thermal diffusion in an adiabatic mantle, and (3) the global mean depth of the 410-km discontinuity, we choose a constant temperature of 1520°C at 400 km depth (i.e., the actual base of the numerical domain). Modeling of the depth-dependent adiabatic gradient in the upper mantle and partial melting beneath a MOR show that the above temperature is also consistent with estimations of "normal" potential temperatures of around 1300–1380°C at MORs [e.g., *McKenzie and Bickle*, 1988; *Langmuir et al.*, 1992; *Asimow et al.*, 2001; *Kushiro*, 2001] (see also Appendix A).

[17] To avoid unrealistic discontinuities in the thermal gradient at the base of the lithosphere, a temperature buffer is applied between the lithospheric (conductive-dominated) and sublithospheric (convective-dominated) domains. This buffer plays the role of forcing a continuous variation of temperature between these two domains and corresponds to the rheologically active layer described in the previous section. The temperature at the bottom of the buffer is set to 1400°C.

[18] The condition of a constant basal temperature T_B = 1520°C at z_B = 400 km is only imposed when the actual temperature gradient below the buffer (i.e., $(T_B - T_{TBL})/(z_B - z_{TBL})$, where T_{TBL} and z_{TBL} are the temperature at the base of the buffer and its depth, respectively) is within the expected range of $0.35 < dT/dz < 0.50$ °C km^{-1} [*Schubert et al.*, 2001]. This condition is not satisfied in lithospheres thicker than ~160 km, where the gradient becomes too steep. When this is the case, the basal temperature is calculated assuming a constant gradient dT/dz = 0.5°C km^{-1}, which translates into maximum lateral temperature variations of ~120 °C at the base of the model. Although this approximation may lack thermodynamic rigorousness, it is consistent with seismic observations on the topography of the 410-km discontinuity that indicate maximum temperature variations of a few hundreds degrees at these depths [e.g., *Flanagan and Shearer*, 1999; *Chambers et al.*, 2005, and

Table 2. Solution Notation and Formulae[a]

Symbol	Solution	Formula
Ol	olivine	$[Mg_xFe_{1-x}]_2SiO_4$
Opx	orthopyroxene	$[Mg_xFe_{1-x}]_{2-y}Al_{2y}Si_{2-y}O_6$
Sp	spinel	$Mg_xFe_{1-x}Al_2O_4$
Cpx	clinopyroxene	$Ca_{1-y}[Mg_xFe_{1-x}]_{1+y}Si_2O_6$
Gt	Garnet	$Fe_{3x}Ca_{3y}Mg_{3(1-x+y+z/3)}$ $Al_{2-2z}Si_{3+z}O_{12}$; $x+y+4z/3 \leq 1$
C2/c	pyroxene	$[Mg_xFe_{1-x}]_4Si_4O_{12}$
Ring	ringwoodite	$[Mg_xFe_{1-x}]_2SiO_4$
Wad	wadsleyite	$[Mg_xFe_{1-x}]_2SiO_4$

[a] From *Stixrude and Lithgow-Bertelloni* [2005a]. Unless otherwise noted, the compositional variables x, y, and z may vary between zero and unity and are determined as a function of the computational variables by free-energy minimization.

references therein]. Moreover, these studies also show that the thermal structure of the upper mantle exerts some influence on the temperature distribution along the discontinuity, as evidenced by upward displacements of the discontinuity in many cratons and downward displacements in some oceans and hotspots (see Appendix B).

3.2. Thermodynamic Modeling and Density Calculation

[19] Stable mineral assemblages in upper mantle domains are computed using a Gibbs free-energy minimization algorithm (see details given by *Connolly* [2005]) within the system CaO-FeO-MgO-Al_2O_3-SiO_2 (CFMAS). Since 98% of the Earth's mantle is made up of these five oxide components [cf. *Palme and O'Neill*, 2005], the CFMAS system is considered to be an excellent basis for modeling mantle phase equilibria. Hence, each mantle body in LitMod is characterized by a particular CFMAS composition (included in the input file). There is evidence, however, that other minor components such as Cr_2O_3 and Na_2O can perturb the system to some extent. Na_2O would somewhat modify the relative amounts of orthopyroxene and clinopyroxene, particularly at $P > 9$ GPa [*Stixrude and Lithgow-Bertelloni*, 2005a]. The addition of Cr_2O_3 is known to broaden the stability field of spinel [e.g., *Klemme and O'Neill*, 1998; *Klemme*, 2004], although the absolute pressure interval of the spinel+garnet stability field in rocks containing clinopyroxene may not be as large as inferred from simplified laboratory experiments [*Webb and Wood*, 1986]. The thermodynamic database we use here [*Stixrude and Lithgow-Bertelloni*, 2005a] does not account for Cr_2O_3, but it predicts plagioclase-spinel-garnet phase transitions that are consistent to a first order with experimental data on natural peridotites with a wide range of compositions [e.g., *Green and Ringwood*, 1970; *Webb and Wood*, 1986; *Green and Falloon*, 1998]. Solution models used in the energy minimization procedure are listed in Table 2.

[20] Equilibrium assemblages at temperatures <500°C are not considered here due to the lack of reliable quantitative information on reaction kinetics and metastability at such low temperatures. Thermophysical properties of these low-temperature assemblages are thus computed at the temperatures and pressures of interest, but the assemblage and phase compositions are assumed to be identical to those at $T = 500$°C.

[21] LitMod allows density calculations of mantle rocks with two different approaches. The user needs to define which one is to be used in the input file. The first approach (hereafter EMA) retrieves density values directly and self-consistently from the energy minimization procedure. The thermodynamic database used in this approach is that of *Stixrude and Lithgow-Bertelloni* [2005a], which is based on a third-order Birch-Murnaghan EoS (the associated thermodynamic framework is described in detail by *Stixrude and Bukowinski* [1990] and *Stixrude and Lithgow-Bertelloni* [2005a, 2005b]). However, recent experimental results indicate that fourth-order effects (not included in EMA) are important in orthopyroxenes [e.g., *Flesch et al.*, 1998; *Kung et al.*, 2004]. To account for this, compressions can optionally be computed from a fourth-order Birch-Murnaghan EoS (hereafter ECA) for each end-member using experimentally derived parameters. The equilibrium compositions of the phases are retrieved from the energy minimization procedure. These compositions are then used to estimate the amount of end-members present in each phase by solving $(C^TC)\,X = C^TB$, where C is the $5 \times m$ end-member compositional matrix, C^T its transpose, B the 5×1 phase compositional matrix, X the $m \times 1$ end-member mass proportions matrix, and m the number of end-members (it varies with analyzed phase). Hybrid methods such as the ECA, where

phase equilibria calculations are supplemented with higher-order derivatives of some properties, are not strictly self-consistent. End-members and associated parameters used in the ECA approach are listed in Table 3.

[22] The fourth-order Birch-Murnaghan EoS is

$$P = 3K_0 f_E (1+2f_E)^{5/2}\left\{1+\frac{3}{2}(K_0'-4)f_E+\frac{3}{2}\cdot\left[K_0K_0''+(K_0'-4)(K_0'-3)+\frac{35}{9}\right]f_E^2\right\} \quad (3)$$

with

$$f_E = \frac{1}{2}\left[(\rho/\rho_0)^{2/3}-1\right] \quad (4)$$

where ρ is the density of a certain end-member mineral at the pressure of interest, and ρ_0, K_0, K_0', and K_0'' are respectively the density, bulk modulus, and its first and second pressure derivatives at $P = 0$ and at a given reference temperature. The more popular third-order version of this EoS is obtained from equation (3) by setting $f_E^2 = 0$. Equation (3) is solved iteratively for ρ with a maximum error of 1×10^{-5} kg m^{-3}. To explicitly include the temperature effect, the above parameters are replaced with $\rho_{0(T,\,0)}$, $K_{0(T,\,0)}$, $K'_{0(T,\,0)}$, and $K''_{0(T,\,0)}$, which still give the corresponding quantities at $P = 0$, but at an arbitrary temperature T. The temperature effect on $K_{0(T,\,0)}$ and $\rho_{(T,\,0)}$ is introduced as

$$K_{0(T,\,0)} = K_{0(T_r,\,0)} + \left(\frac{\partial K_{0(T,\,0)}}{\partial T}\right)_P (T-T_r) \quad (5a)$$

$$\rho_{(T,\,0)} = \rho_{(T_r,\,0)} \exp\left(-\int_{T_r}^{T} \alpha(T)dT\right) \quad (5b)$$

where $K_{0(Tr,\,0)}$, $\rho_{(Tr,\,0)}$, and $\alpha(T)$ are the isothermal bulk modulus at $T = T_r$ (usually 300 K) and ambient pressure, the density at $T = T_r$, and the coefficient of thermal expansion as a function of T, respectively. For the latter, the usual polynomial functions are used [cf. *Fei*, 1995] (see also Table 3). Excepting for orthopyroxene, in which fourth-order effects and nonlinearity of its T-P derivatives have been reported [e.g., *Flesch et al.*, 1998; *Kung et al.*, 2004; *Jackson et al.*, 2007], the third-order version of equation (3) is used with $K_{0(T,\,0)}'$ and $K_{0(T,\,0)}''$ independent of pressure and temperature (a common assumption due to the small values of the second derivatives and the uncertainties associated with them [*Angel*, 2000; *Poirier*, 2000]).

[23] Once the densities of the end-member minerals are obtained, those of the stable phases are estimated following the experimentally constrained model of *Brey et al.* [1999], expanded for clinopyroxene as done by *Lee* [2003]. Plagioclase has a pure An_{100} composition. Finally, the bulk rock density is calculated with the usual rule of mixture $\rho_B = \sum_{i=1}^{i=n} \rho_i v_i$, where n, ρ_i, and v_i are the number of stable phases, and the density and volumetric fraction of the ith phase, respectively. Note that majoritic garnet and pyroxene phase transitions are also included.

[24] Predictions from these two approaches (EMA and ECA) for a range of compositions have been compared to evaluate the uncertainties in our density calculations. As expected, discrepancies are insignificant at low pressures (0.2% at $P < 6$ GPa) and increase with depth. The ECA predicts systematically higher densities than the EMA due to the slightly different thermodynamic parameters used in each approach. Nevertheless, differences in predicted densities are always <0.6% for the entire depth range 0–400 km ($0 < P$ 13.3 GPa).

3.3. Density and Pressure at Each Node

[25] The final density and pressure at each node of the model are obtained with an iterative scheme (see Figure 1). Within the crust, where mineral equilibria are not solved for, the density is calculated with the following formula:

$$\rho_{(T,P)} = \rho_\circ - \rho_\circ\alpha(T-T_\circ) + \rho_\circ\beta(P-P_\circ) \quad (6)$$

where α and β are the coefficient of thermal expansion and compressibility, respectively. For the different mantle domains, density is obtained as described above. The pressure is calculated at every node in all columns from the surface to the bottom. Every time a new node is added (downward), the pressure is calculated as a function of the overburden pressure with the usual lithostatic equation ($P = \overline{\rho_l(z)}g\,z$). This pressure is then used to obtain the P-T-dependent density at the node; this density then is used in the next iteration to update the overburden pressure and to solve for an updated density. The iteration stops when the density difference between two consecutive iterations (i.e., $\rho_{n-1} - \rho_n$) is ≤ 0.01 kg m^{-3}. If the vertical separation between nodes is small (numerical tests suggest <4.4 km), the system converges to the desired accuracy in only two or three iterations.

Table 3 (Sample). Thermodynamic Parameters of Relevant Minerals[a] [The full Table 3 is available in the HTML version of this article at http://www.g-cubed.org]

Mineral	Symbol	Formula	a, 10^{-5}	b, 10^{-8}	c,	d, 10^{-18}	Formula Weight	Molar Vol., $cm^3\ mol^{-1}$	K_S, GPa	$K_{0(Tr,\ 0)}$, GPa	G, GPa	dK_S/dT, GPa K^{-1}
Forsterite	Fo	Mg_2SiO_4	2.85	1.008	−0.384		140.691	43.63	128.8	127.4	81.2	−0.017
Fayalite	Fa	Fe_2SiO_4	2.386	1.153	−0.0518		203.771	46.35	138	136.6	50.9	−0.0204
Orthoenstatite	Oen	$Mg_2Si_2O_6$	2.947	0.57			200.774	62.676	102.35	101.5	75.5	−0.0217(−7.18)[b]
Orthoferrosilite	Ofs	$Fe_2Si_2O_6$	3.08	0.978	−0.4	1.52	263.86	65.941	101	100.2	52	−0.0217(−7.18)[b]
Mg-Tshermaks	Mg-Ts	$MgAlAlSiO_6$	2.947	0.6			202.346	60.4	181	179.5	114	−0.027
Mg-Cr-Tshermaks	Mg-Cr-Ts	$MgCrAlSiO_6$	2.947	0.6			227.361	61.4	181	179.5	114	−0.027
Diopside	Di	$CaMgSi_2O_6$	2.6[c]	1.15	−0.5		216.56	66.039	113	112.2	67	−0.0123
Hedenbergite	Hd	$CaFeSi_2O_6$	2.6[d]	1.15	−0.5		248.1	67.867	119	117	61	−0.02
Jadeite	Jd	$NaAlSi_2O_6$	2.56	0.26			202.14	60.508	125	125	85	−0.017
Mg-diopside	Mg-Di	$MgMgSi_2O_6$	2.6[d]	1.15	−0.5		200.77	63.16	113	112.2	67	−0.0123
Pyrope	Py	$Mg_3Al_2Si_3O_{12}$	2.311	0.5956	−0.4538		403.15	113.08	172.73	171.32	92	−0.0191
Grossular	Gr	$Ca_3Al_2Si_3O_{12}$	1.1951	0.889	−0.6617		450.439	125.12	166.82	165	108.9	−0.0148
Knorringite	Kn	$Mg_3Cr_2Si_3O_{12}$	2.311	0.5956	−0.4538		453.15	117.38	172.73	171.32	92	−0.0191
Almandine	Alm	$Fe_3Al_2Si_3O_{12}$	1.776	1.214	−0.5071		497.76	115.43	175	173.3	97.7	−0.0204
Uvarovite	Uv	$Ca_3Cr_2Si_3O_{12}$	2.232	0.5761	−0.2329		500.48	129.71	162	160	92	−0.0148
Majorite	Mj	$Mg_4Si_4O_{12}$	2.311	0.5956	−0.4538		401.548	113.99	166	164.7	85	−0.019
HP-clinoenstatite	HP-Cen	$Mg_2Si_2O_6$	2.2[e]	2.1			200.774	60.61	123	121.7	88	−0.017
HP-clinoferrosilite	HP-CFs[f]	$Fe_2Si_2O_6$	2.2	2.1			263.86	64.08	123	121.7	88	−0.017
Spinel	Sp	$MgAl_2O_4$	1.87	0.975	−0.365		142.27	39.75	199.6	197.5	108.2	−0.0186
Chromite	Chr	$FeCr_2O_4$	0.97	1.9392			223.84	44.41	203	201	105	−0.0186
Picrochromite	Pchr	$MgCr_2O_4$	0.97	1.9392			192.3	43.564	203	201	105	−0.0186
Hercynite	Hcy	$FeAl_2O_4$	0.513	1.5936			173.81	40.843	210.3	208.3	84	−0.0186
Plagioclase	Plg	$CaAl_2Si_2O_8$	1.394[g]	0.0597			278.36	100.61	82.5	82.5	38.8	−0.018

[a] Note that Na and Cr end-members are not relevant for the present work, but we include them here for completeness. $\alpha(T) = a + b*T + c/T^2 + d*T^4$. Most values from = compilations of *Lee* [2003], *Matsukage et al.* [2005], and *Schutt and Lesher* [2006], except for the following: Fo, Fa, dK_T/dT [from *Suzuki et al.*, 1998]; dK_S/dP and dG/dP of Fa [from *Speziale et al.*, 2004]; dK_T/dP of Fa (average from works in Table 4.1 of *Poirier* [2000]). OEn: Parameters from *Kung et al.* [2004] and *Jackson et al.* [2007]. Di: dK_S/dT, dK_T/dT, dG/dT from *Isaak et al.* [2006]. Jd: dK_S/dP from *Zhao et al.* [1997]. Py: dK_T/dT and dG/dT from *Gwanmesia et al.* [2006]. Gr: dK_T/dT from *Pavese et al.* [2001]. HP-CEn: K_S and K_T extrapolated from *Kung et al.* [2004, 2005]. Plg: parameters for EoS from *Angel* [2004], assuming a composition An_{100}; other parameters assumed.

[b] Values in parentheses are in 10^{-6} [GPa K^{-2}]. The moduli are calculated as $M = M_0 + M_1(T\text{-}294) + M_2\ (T\text{-}294)^2$, where M_1 are the first values given in the table and M_2 are the values in parentheses. Temperature in degrees Kelvin [*Jackson et al.*, 2007].

[c] From *Isaak et al.* [2006].

[d] Same as in Di.

[e] From *Shinmei et al.* [1999].

[f] Same as in HP-CEn.

[g] From *Fei* [1995] for Plg Ab_5 An_{95}.

3.4. Potential Fields: Gravity and Geoid Anomalies

[26] Free-air and Bouguer gravity anomalies in two dimensions are calculated using the algorithm for polygonal bodies of *Talwani et al.* [1959]. This algorithm is applied to each element of the mesh, and therefore it accounts for both lateral and vertical density variations within the bodies. The gravity effect of all the elements is then added and calculated either at the top of the model or at the sea level, depending on if the elevation is above or below sea level, respectively. In order to avoid boundary effects, the models are extended horizontally 1×10^5 km beyond the profile limits. Due to the $1/r^2$ dependency of the gravity field, where r is the distance to the density anomaly, gravity anomalies basically provide information on the density distribution at crustal and shallow subcrustal depths (the short-wavelength part of the signal). Geoidal height, on the other hand, is more sensitive to deeper density anomalies and to the topography of the LAB. This is mainly due to the fact that the geoid anomaly is the height difference between two equipotential surfaces, and therefore it is a function of $1/r$ instead of $1/r^2$, where r is the distance to the density anomaly [*Turcotte and Schubert*, 1982].

[27] The calculation of the geoid height is done by converting two adjacent triangular elements of the mesh into rectangular prisms throughout the model, solving the integral of the their gravity potential, and substituting the result into Brun's formula ($\Delta N = \Delta U/g_o$, where ΔN is the geoid anomaly, ΔU the potential anomaly, and g_o the normal gravity acceleration). One finally obtains

$$\Delta N = \frac{G.\rho}{g_\circ} \int_{x_1}^{x_2} \int_{y_1}^{y_2} \int_{z_1}^{z_2} \frac{1}{\sqrt{x^2+y^2+z^2}} dz\, dy\, dx \qquad (7)$$

where G is the gravitational constant, and x, y, and z the coordinates of the prism boundaries. LitMod uses the method outlined by *Zeyen et al.* [2005], based on an analytical solution of equation (7), to obtain 2.5-D geoid heights along the model. The length in the direction of the y-axis (i.e., section thickness) is taken for all the models to be large enough to simulate two-dimensional anomalies.

[28] The classic 1-D isostatic geoid formulation given by *Turcotte and Schubert* [1982] can be calculated simultaneously or alternatively. It reads as

$$\Delta N = -\frac{2\pi G}{g_\circ} \int_0^h z \triangle \rho(z) dz \qquad (8)$$

where h is the maximum depth of the model.

[29] Throughout the process, the model is assumed to be in isostatic equilibrium to avoid undesired border effects in the calculated geoid. This condition is implicitly fulfilled if the model fits elevation data.

3.5. Seismic Velocities

[30] The calculation of seismic velocities ($V_p^2\rho = K_S + 4/3G$ and $V_s^2\rho = G$) requires knowing the elastic moduli of each end-member mineral and the density of the bulk rock at the pressures and temperatures of interest. Densities are obtained as described in section 3.2, while the elastic moduli of the aggregate (i.e., rock) are computed as follows. First, the amounts of end-members (mole fractions) present in each stable phase are retrieved from a least squares procedure as explained in section 3.2 (i.e., $(C^TC)\ X = C^TB$). The moduli of each solution phase are then calculated as the arithmetic mean of the end-member moduli weighted by their respective molar proportions (appropriate for chemical mixtures [e.g., *Connolly and Kerrick*, 2002]). Elastic moduli and their T-P derivatives are summarized in Table 3 for end-member minerals.

[31] In a second step, the elastic moduli of the bulk rock are computed following a Voigt-Reuss-Hill (VRH) average scheme [*Hill*, 1952]

$$M_B = \frac{1}{2}\left[\left(\sum_{i=1}^{n} w_i/M_i\right)^{-1} + \sum_{i=1}^{n} w_i M_i\right] \qquad (9)$$

where M_i and w_i are the moduli of the phases present (computed in the previous step) and their volumetric fractions, respectively. Except for some garnet pyroxenites and eclogites, for which we use the model of *Afonso et al.* [2005], differences between the VRH scheme and other more sophisticated methods such as the Hashin-Shtrikman [*Hashin and Shtrikman*, 1963] or the modified shear-lag [*Afonso et al.*, 2005] are negligible given the uncertainty in end-member moduli and modal proportions. More detailed discussions on the theory of composites applied to polycrystalline rocks are given by *Ji et al.* [2003] and *Afonso et al.* [2005].

[32] In its present version, LitMod does not explicitly consider either anisotropy or anelasticity. The former is subject to many uncertainties and strong local variability [e.g., *Gung et al.*, 2003], and therefore a general treatment of this effect is of little value for the purpose of this paper. The latter, on the

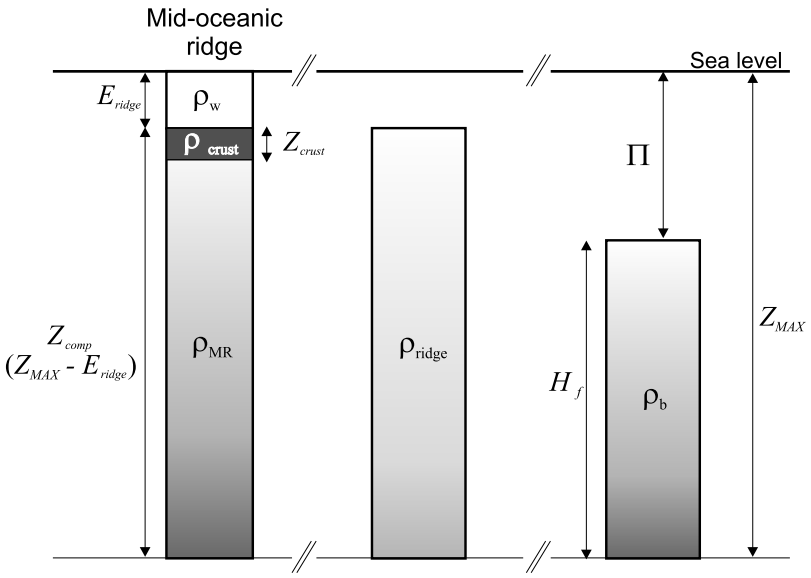

Figure 2. Isostatic balance used to calculate the absolute elevation of different columns with respect to a reference column at a MOR. E_{ridge}, ridge elevation (−2.6 km); Z_{crust}, crustal thickness (7 km); Z_{MAX}, model's maximum depth (400 km); ρ_w, density of seawater (1030 kg m^{-3}); ρ_{crust}, density of oceanic crust (2930 kg m^{-3}); ρ_{MR}, depth-averaged density of mantle below the MOR; ρ_{ridge}, depth-averaged density of the MOR (crust + mantle); ρ_b, density of the mantle at $z = Z_{\mathrm{MAX}}$. Refer to text for the meaning of parameters H_f and Π.

other hand, is of primary importance due to its sensitivity to temperature and melt anomalies [*Sobolev et al.*, 1996; *Goes et al.*, 2000; *Cammarano et al.*, 2003]. Inferences on possible compositional heterogeneities from seismic data also require an adequate estimation of anelastic attenuation (see section 4.3). We compute anelastic effects *a posteriori* as a function of grain size (d), oscillation period (T_o), temperature (T), pressure (P), and empirical parameters A, E, and α as [e.g., *Karato*, 1993; *Afonso et al.*, 2005]

$$V_p = V_{p_\circ}(T,P)\left[1 - \left(\frac{2}{9}\right)\cot\left(\frac{\pi\alpha}{2}\right)Q_s^{-1}\right] \tag{10a}$$

$$V_s = V_{s_\circ}(T,P)\left[1 - \left(\frac{1}{2}\right)\cot\left(\frac{\pi\alpha}{2}\right)Q_s^{-1}\right] \tag{10b}$$

where we assumed $Q_p = 9/4\ Q_s$ (i.e., $Q_K^{-1} \sim 0$). $V_{p_o}(T,P)$ and $V_{s_o}(T,P)$ are the unrelaxed high frequency wave velocities at a given temperature and pressure, and

$$Q_s^{-1} = A\left[T_o d^{-1}\exp\left(\frac{-E+VP}{RT}\right)\right]^{\alpha} \tag{11}$$

with $A = 750$ s$^{-\alpha}\mu$m$^{\alpha}$, $\alpha = 0.26$, $E = 424$ kJ mol^{-1}, $V = 1.2 - 1.4 \times 10^{-5} m^3$ mol^{-1}, and R the universal gas constant [*Jackson et al.*, 2002; *Faul and Jackson*, 2005]. We ignore the effect of water on seismic velocity through enhancement of attenuation. This effect is important above subducting plates or plumes [*Karato*, 2003], but it is not clear if it plays a significant role in ocean basins or continental lithosphere (which is likely to be depleted of water) not affected by hot-spot volcanism or subduction [*Karato*, 2003; *Faul and Jackson*, 2005].

3.6. Elevation

[33] Local isostasy has been proven to be a suitable approximation in regions where short-wavelength, elastically supported features such as buried and/or topographic loads are not present [*Turcotte and Schubert*, 1982; *Watts*, 2001; *Hasterok and Chapman*, 2007]. According to the principle of isostasy, all regions of the Earth with identical elevation must have the same buoyancy when referenced to a common compensation level. We assume here that the latter is located at the base of the model (∼410-km discontinuity). The choice of a global compensation level at this depth has two advantages: (1) it covers the whole range of estimated lithospheric thicknesses, and (2) there is no need to change the calibration constants for different models (see below). The physical rationale behind this assumption and a discussion of its limitations are given in Appendix B.

[34] In order to estimate absolute elevation one needs to perform a calibration with respect to a reference column (Figure 2). We take this reference column at a mid-oceanic ridge (MOR), where average elevations, petrogenetic processes, and lithospheric structures are known in greater detail than in any other tectonic setting (see section 3.6.2 and Appendix A). The final formulae that LitMod solves to obtain absolute elevation are similar to those of *Lachenbruch and Morgan* [1990], where the elevation above (E_a) and below (E_b) the sea level are given respectively by

$$E_a = \int_{L_{top}}^{L_{bottom}} \frac{\rho_b - \rho_l(z)}{\rho_b}\, dz - \Pi \tag{12}$$

$$E_b = E_a \frac{\rho_b}{\rho_b - \rho_w} \tag{13}$$

where L_{top} is taken at the top of the column, L_{bottom} is taken at the bottom of the column, ρ_b (assumed constant) is the density of the mantle at 400 km depth, $\rho_l(z)$ is the depth-dependent density, ρ_w is the density of seawater (=1030 kg m^{-3}), and Π is a calibration constant. Although equations (12) and (13) are formally identical to those of *Lachenbruch and Morgan* [1990], the meanings of some parameters are completely different and should not be confused. Equations (12) and (13) can be solved for any particular model if the forms of the functions $\rho_l(z)$ for every column and the value of Π are known. The term $\rho_l(z)$ is obtained as described in section 3.2. In the following we explain how to obtain the Π parameter.

3.6.1. Parameter Π

[35] In order to calculate Π, the average density, lithospheric structure, and the elevation of a reference column are required. Referring to Figure 2, the mean density of the water-unloaded ridge column is

$$\rho_{ridge} = \frac{\left(Z_{comp} - Z_{crust}\right) \times \rho_{MR} \quad + \quad \left(Z_{crust} \times \rho_{crust}\right)}{Z_{comp}} \tag{14}$$

Therefore, from equations (12) and (13) and Figure 2 one can write

$$\Pi = Z_{\mathrm{MAX}} - \frac{\left(\rho_{ridge} \times Z_{comp}\right) + \left(E_{ridge} \times \rho_w\right)}{\rho_b} \tag{15}$$

Equation (15) shows that the Π parameter is the depth (from sea level) of a fictitious column of height H_f that has a mean density ρ_b (Figure 2). Note that Π is dependent on Z_{MAX}, and hence it takes different values for different compensation levels. Since the mean density ρ_b also changes with depth, the overall effect of choosing a different compensation level is nil for elevation estimations (i.e., Z_{MAX} and ρ_b counterbalance each other). This allows the choice of different compensation depths for the same model while still deriving the same elevation, provided the new ρ_b and Π for that particular compensation depth are recalculated.

3.6.2. Ridge Model

[36] The two most important inputs for calculating the elevation of our model are ρ_b (the basal density) and ρ_{MR} (the average density of the MOR, including crust and mantle). Both values can be obtained by modeling the density distribution with depth under a MOR. Although the MOR model presented in this section relies mostly on well-known data, it is acknowledged that other necessary information may reflect the actual state of knowledge.

[37] There are eight main factors that need to be taken into account when calculating the final density distribution with depth in a MOR column, namely, (1) composition of the source ("undepleted" mantle), (2) solid phase compressibility, (3) melt compressibility, (4) total amount of partial melting (F), (5) depth-distribution of melt ($F(z)$), (6) chemical variation of both solid and melt phases versus degree of partial melting, (7) solid-state phase transitions, and (8) temperature gradient. For the first factor we assume the PUM major-element composition of *McDonough and Sun* [1995] (see Table 1). It will be shown that this model composition predicts seismic velocities and densities that are in good agreement with those given by seismological models. Other common compositional models of the upper mantle [e.g., *Niu*, 1997, and references therein] produce identical results. The second factor was discussed in section 3.2, and the same approach is used here. The last six factors are closely related to each other, and therefore they can be estimated in a coherent manner by assuming a particular ridge model (the full treatment of this model is presented in Appendix A).

[38] The final model for the MOR column obtained with the aforementioned considerations is shown in

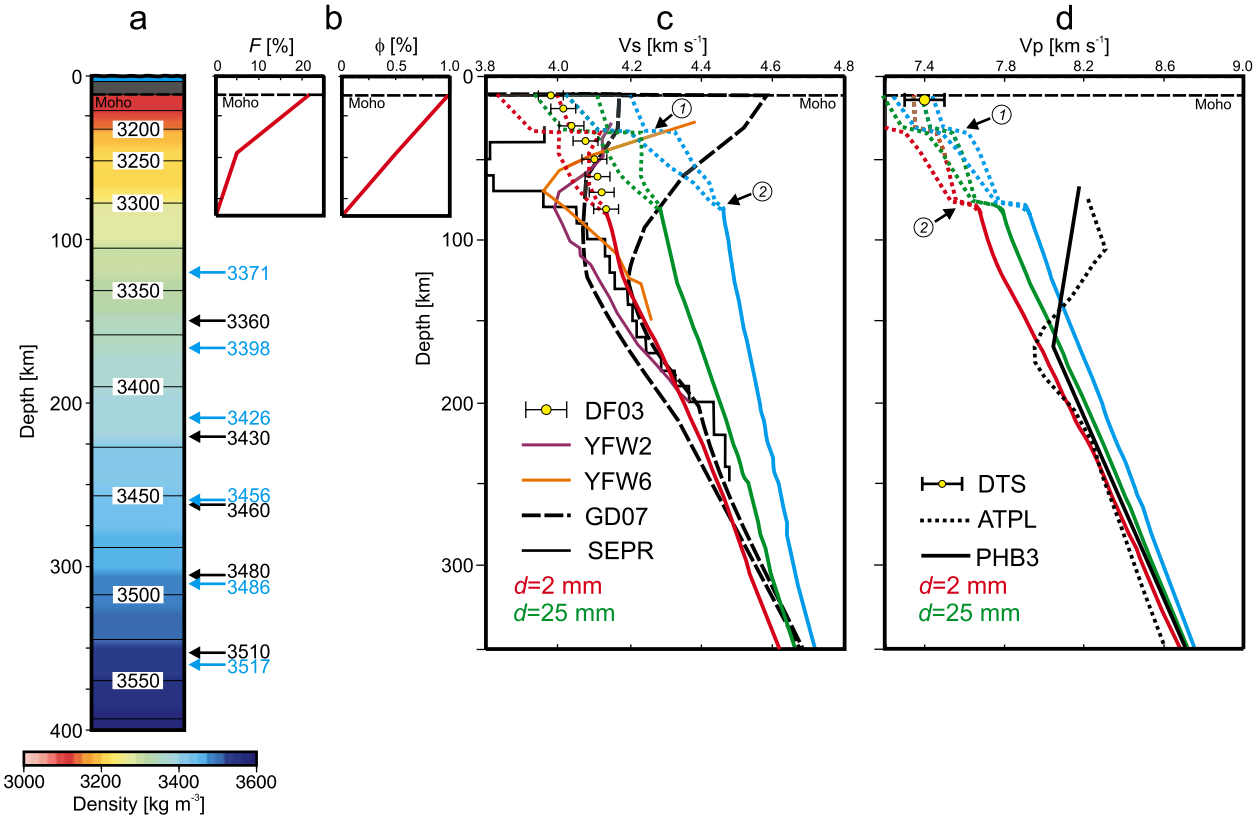

Figure 3. (a) Modeled density distribution of the reference column at a MOR. Contours are in kg m^{-3}. The arrows indicate density values from seismological models at those depths: black arrows are from PREM [*Dziewonski and Anderson*, 1981]; blue arrows are from *ak*135 [*Kennett et al.*, 1995]. (b) Melt depletion (F) and porosity (ϕ) distribution with depth used to estimate the final density of column A. (c) Modeled isotropic Vs velocities beneath a MOR. Color lines denote purely elastic approximation (blue) and anelastic approximation with a grain size d = 2 mm (red) and d = 25 mm (green). The attenuation effect is computed for a representative frequency of 15 mHz [*Gaherty and Dunn*, 2007] and $V = 1.25 \times 10^{-5}$ m^3 mol^{-1}. Color dotted lines include the effect of free melt [*Hammond and Humphreys*, 2000]. Arrows denote the following phase transitions: 1, plagioclase-spinel; 2, spinel-garnet. The DF03 is the model of *Dunn and Forsyth* [2003] at the ridge axis (East Pacific Rise) and associated uncertainties. The YFW2 and YFW6 are the velocity profiles of *Yang et al.* [2007] in the southern East Pacific Rises for plate ages of 2 and 6 Ma, respectively. The GD07 are envelopes containing values given by *Gaherty and Dunn* [2007] for oceanic lithospheres ~5–10 Ma old. The SEPR model is that of *Gu et al.* [2005] for the southern East Pacific Rise. (d) Modeled isotropic Vp velocities beneath a MOR. Color lines as in Figure 3c. Values from seismological models PHB3 [*Gaherty et al.*, 1999] and ATLP [*Zhao and Helmberger*, 1993] are shown for comparison. DTS value is from *Dunn et al.* [2000] at the ridge axis (East Pacific Rise) and associated uncertainties. See text and Appendix A for details.

Figure 3a. Density estimations from spherically symmetric seismological models PREM [*Dziewonski and Anderson*, 1981] and *ak*135 [*Kennett et al.*, 1995] are included for comparison. We emphasize that this idealized ridge column is constructed only for the purpose of serving as a calibration constant. Therefore, although it is consistent with all available petrological and geophysical information, comparisons with particular MOR settings need to be taken with caution (see below). The average mantle density of the MOR column (ρ_{MR}), needed for the isostatic model, is readily obtained by numerical integration of the density with respect to depth. Figure 3 also shows the velocity profiles predicted by our MOR model together with those from seismological models in young oceanic environments GD07 [*Gaherty and Dunn*, 2007], YFW2-YFW6 [*Yang et al.*, 2007], SEPR [*Gu et al.*, 2005], DF03 [*Dunn and Forsyth*, 2003], PHB3 [*Gaherty et al.*, 1999], and ATLP [*Zhao and Helmberger*, 1993]. Anelastic attenuation effects were included as explained in section 3.5 for a representative frequency of 15 mHz [*Gaherty and*

Dunn, 2007] and an activation volume $V = 1.25 \times 10^{-5}$ m^3 mol^{-1}. Dotted lines include the effect of free melt ϕ (plotted in Figure 3b) on seismic velocities based on the results of *Hammond and Humphreys* [2000]. The two dotted lines in each solid curve represent the minimum (1.2% for Vp, 2.7% for Vs) and maximum (3.6% for Vp, 7.9% for Vs) velocity reductions calculated by *Hammond and Humphreys* [2000] for melt fractions $\leq$1%.

[39] At depths >150 km, all models agree relatively well. As previously found [*Faul and Jackson*, 2005], an increase of the grain size with depth would reproduce seismic data satisfactorily at depths >100 km. At shallower depths, our results for an ideal MOR (including the decrease in Vs due to the presence of melt) have no realistic counterparts in most available seismological models, which commonly include the effect of a thin cooled lid above ~50 km (e.g., YFW2, YFW6, and SEPR). The model of *Dunn and Forsyth* [2003] constitutes a relevant exception. By inverting short-period Love waves, these authors produced a structural model of shear wave velocity beneath the East Pacific rise from the Moho to ~150 km depth. The resulting 1-D velocity profile at the ridge axis is plotted in Figure 3c (DF03). Within uncertainties, our ideal ridge model with a grain size of 2 mm is remarkably similar to the seismological model, although the latter does not show the velocity jump predicted at the plagioclase-spinel phase transition (the deeper spinel-garnet phase transition is hardly noticeable in Vs). This discrepancy could be the result of at least three different factors: (1) the velocity of the ascending material beneath the ridge is high enough to make the two-phase region wider, thus diminishing the velocity contrast of the discontinuity [cf. *Schubert et al.*, 2001] (see also section 4.3.1); (2) the amount of partial melting (depletion) experienced by the ascending material at the transition depth is large enough to remove most of the original Ca and Al from the solid residue (two highly incompatible elements), thus reducing considerably the amount of plagioclase and spinel that can be formed; and (3) the amount of melt present below the transition is somewhat higher than that above the transition and cancels out the velocity decrease. A combination of these is also plausible. Inasmuch as our method cannot account for dynamic effects, we are not able to discriminate between these potential factors. However, considering that the East Pacific Rise is a fast spreading ridge (>110 mm a^{-1}), factors 1 and 2 are expected to occur to some extent beneath the ridge. The third factor is more uncertain, but the changes in volume and in the solidus slope associated with the phase transition [*Asimow et al.*, 2001; *Kushiro*, 2001] could in principle cause this effect.

[40] When we compare our results for the ideal ridge with seismological models in young oceanic lithosphere, considerable differences emerge. Models YFW2, YFW6, and SEPR in Figure 3c are all representative of oceanic lithosphere ~2–6 Ma old in the south East Pacific Rise. These models show that oceanic plates develop a high-velocity conductive lid after only a few Ma, a feature absent in our ideal ridge model. Also, a large decrease in shear velocity is observed at depths between 40–80 km. We discuss these features in more detail in the next section.

4. Application to the Oceanic Lithosphere

[41] Although there still is some debate as to which model better describes the thermal structure of "normal" oceanic lithosphere, its evolution is relatively simple and well understood. It is generally accepted that the oceanic lithosphere represents a cold thermal boundary layer above an approximately adiabatic mantle. However, some key questions regarding the structure of the oceanic upper mantle are still subject to controversy; foremost among these are the compositional layering of oceanic plates and their average degree of depletion, the origin of the "steady-state" thermal structure and seafloor topography, its buoyancy with respect to the underlying sublithospheric mantle, the importance of attenuation on seismic tomography interpretation, and the origin of the low velocity zone (LVZ). A number of recent papers addressed these topics individually using different approaches [e.g., *Niu*, 2004; *Ritzwoller et al.*, 2004; *Faul and Jackson*, 2005; *Huang and Zhong*, 2005; *Stixrude and Lithgow-Bertelloni*, 2005a; *Priestley and McKenzie*, 2006; *Afonso et al.*, 2007; *Simon et al.*, 2008; *Yang et al.*, 2007; Zlotnik et al., submitted manuscript, 2008]. However, we anticipate that all these factors are intimately related, and thus an integrated study that link them in a consistent manner is desirable. This is the objective of the present section.

4.1. Geophysical Observables

[42] Our goal is to study the general features characterizing the normal evolution of the oceanic lithosphere. However, in order to make our model

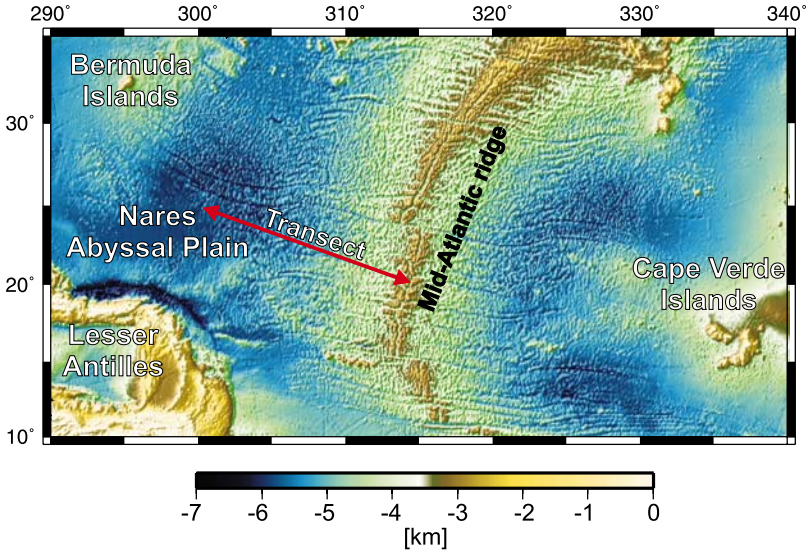

Figure 4. Location map of the transect from which relevant geophysical observables (Figure 6) where extracted. Color scale is elevation in kilometers.

consistent with available geophysical information, we use real geophysical observables (free-air anomalies, geoid height, SHF, seismic velocities, and elevation) as constraints to the final model. Free-air anomalies, geoid height, and elevation are taken from *Sandwell and Smith* [1997], EGM-96 model (properly filtered to avoid deep effects [*Lemoine et al.*, 1998]), and ETOPO 2 [*National Geophysical Data Center*, 2001], respectively. The transect from which the observables are taken runs along ~1500 km, perpendicular to the Mid-Atlantic ridge (Figure 4), passing through oceanic crust 0 Ma to ~90–95 Ma old [*Mueller et al.*, 1997]. This particular transect is the same used by *Afonso et al.* [2007] to study the density structure and buoyancy of oceanic plates. It is preferred over other possible transects for the following reasons: (1) the sedimentary cover is very thin (100 m) (e.g., D. L. Divins, http://www.ngdc.noaa.gov/mgg/sedthick/sedthick.html); (2) effects of local hot-spot swells are minimal (although the Bermuda swell may cause a local increase in bathymetry of ~200–300 m in the oldest part of the transect [*Shahnas and Pysklywec*, 2004]); (3) large-scale dynamic topography is minimal [*Steinberger et al.*, 2001]; (4) the average half-spreading rate is small (~1.7 cm a^{-1}); and (5) lateral variability of geophysical observables in the oldest parts is small. All of the above suggest that anomalous effects in this profile should be minimal. Due to the lack of detailed information regarding the crustal structure along the transect, a simple two-layer model crust 6.8-km thick was assumed. The upper layer is only present between $x = 0$ and $x = 850$ km, and is intended to represent a thin layer of sediments with an average density of 2220 kg m^{-3}. The second layer represents the igneous part of the oceanic crust, with a surface density of 2950 kg m^{-3}.

[43] No reliable SHF data is available along the transect. Again, since we are interested in representative global SHF trends, this is not a serious hindrance for our model. We use therefore global SHF data [*Stein and Stein*, 1992; *Pollack et al.*, 1993] as a constraint for attainable SHF values.

4.2. Petrological Model

[44] The compositional layering of the oceanic mantle is mostly inherited from the melt extraction experienced at the MOR. *Niu* [1997] presented the first quantitative melting model applied to abyssal peridotites. This model predicts the following: (1) the relation between residual mineral modes and the extent of melting follows a quasi-linear trend, and (2) a simple CIPW norm scheme can be used to transform model residue compositions into normative mineral modes [see *Niu*, 1997, Figures 5 and 12]. Results from this model differ from those obtained in isobaric melting experiments in that the former predicts that orthopyroxene contributes more than clinopyroxene to the melt during decompression melting, in contrast to what is observed in isobaric experiments and some model melting reactions [e.g., *Walter*, 1998]. *Niu* [1997] ascribed these discrepancies to the

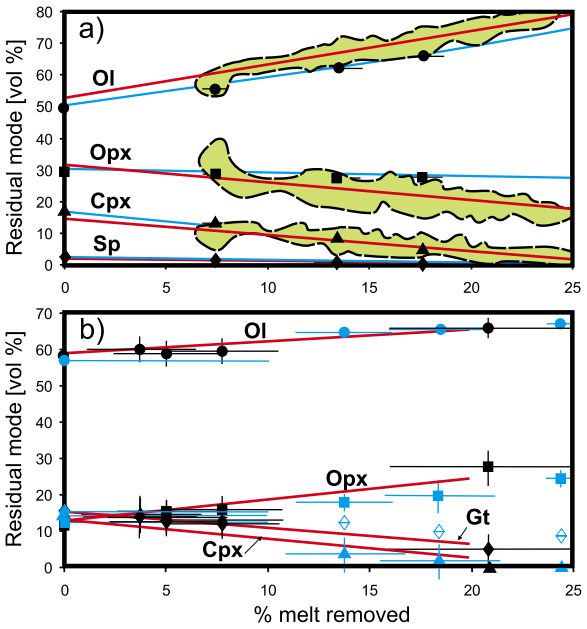

Figure 5. Computed residual modes of spinel and garnet peridotites as a function of melt extraction (red lines). Ol, olivine; Opx, orthopyroxene; Cpx, clinopyroxene; Sp, spinel; Gt, garnet. (a) Residual modes for spinel peridotite in vol %. Blue lines and experimental data at 1 GPa from *Baker and Stolper* [1994]; dashed lines enclose abyssal peridotite data from *Niu et al.* [1997]. Black circles, OL; black squares, Opx; black Triangles, Cpx; black diamonds, Sp. (b) Residual modes for garnet peridotite in vol %. Experimental data and associated uncertainty at 3.6 (black) and 3.0 (blue) GPa from *Lesher and Baker* [1997] and *Walter* [1998], respectively, corrected for the slightly different primitive composition adopted in this work. Unfilled diamonds represent fitting data obtained from this correction but not observed in the experiments. Symbols as in Figure 5a except for diamonds that now represent garnet.

complex *polybaric* nature of decompression melting beneath a MOR, which cannot be reproduced experimentally. *Niu* [1999, 2004] further showed that his model is consistent with modal observations in abyssal peridotites as well as with decompression melting models. We adopt here the same melting model shown in Figures 3 and A1 with the empirical partition coefficients $D_i(F,P)$ of *Niu* [1997] to model the residual major-element composition of the oceanic mantle after melt extraction (see also Appendix A). We further assume a passive flow regime at the MOR. It should be noted that this approach is only valid for a spinel-bearing peridotite, and it needs to be modified when applied to a peridotite within the garnet stability field. When this is the case, we use the experimental results of *Lesher and Baker* [1997] and [*Walter*, 1998], corrected for the slightly different parent source adopted in this work. The resultant modal proportions as a function of melt extraction are shown in Figure 5.

4.3. Results

[45] Figure 6 shows the fit to the observables and the thermal structure of the best fitting model obtained in this work. The resulting density structure is shown in Figure 7. As expected, outputs in terms of temperature and density structures are similar to those obtained by *Afonso et al.* [2007], who applied a similar methodology, but modeled explicitly only the first 300 km of the upper mantle. Thus, we will not discuss further the buoyancy and density structure of the oceanic plate, which are treated in detail in the above paper. Instead, we will focus on the resulting seismological structure of the oceanic lithosphere and underlying mantle, and its implications for the interpretation of tomographic studies and compositional models.

4.3.1. Phase Transitions

[46] Figure 8 shows Vp and Vs synthetic seismic structures of the oceanic upper mantle corresponding to the model in Figure 6. One-dimensional velocity profiles extracted from the same model are shown in Figure 9. It is apparent from Figures 8 and 9 that although both Vp and Vs "see" well the plagioclase-spinel solid-state phase transition, the spinel-garnet transition is only clearly visible in the Vp case (the same can bee seen in our ideal ridge model, Figure 3c). The competing effects of temperature, pressure, and most importantly, modal composition tend to cancel each other across this phase transition, resulting in a relatively smooth Vs velocity profile (see also Figure 9). This result is consistent with the 1-D estimations of *Stixrude and Lithgow-Bertelloni* [2005a], although the magnitude of the velocity jump in their model is slightly larger than in ours (Figure 9). This discrepancy is most likely attributable to the different equilibrium modal assemblages and geotherms between those computed here and those of *Stixrude and Lithgow-Bertelloni* [2005a]. Unlike our model, that of *Stixrude and Lithgow-Bertelloni* [2005a] did not consider compositional changes and/or stratification resulting from melt extraction at the MOR (e.g., Ca and Al extraction), and therefore their mineral assemblages are somewhat different from ours.

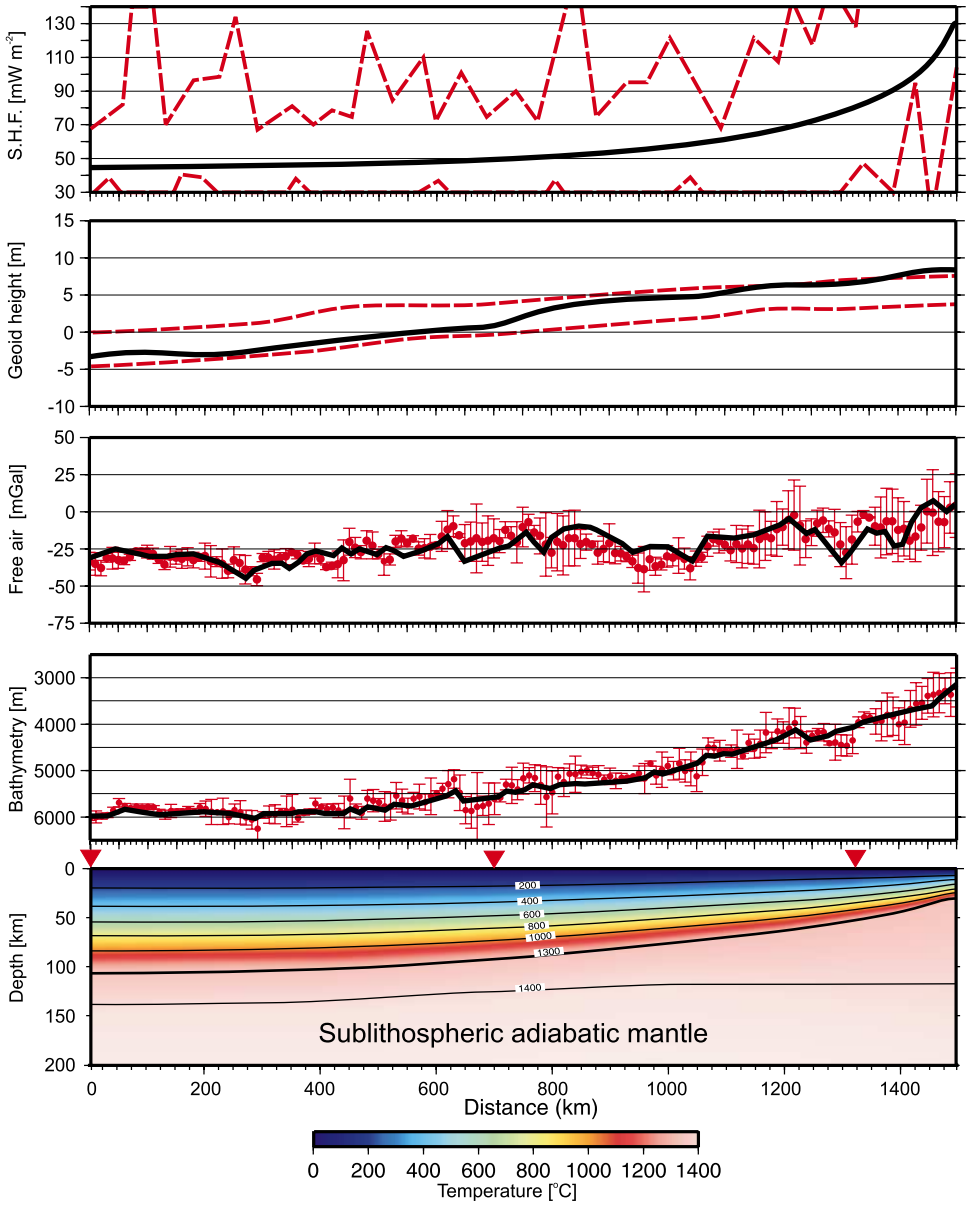

Figure 6. Modeling results of SHF, geoid height, free-air gravity anomalies, and bathymetry. The bottom panel shows the thermal structure of the best fitting model. Red dots and vertical bars denote observed values and associated scatter from global databases along the transect. Black lines represent outputs from the model. Dashed envelope in the SHF is one standard deviation from the mean value for the global data of *Stein and Stein* [1992]. Dashed envelope in the geoid contains commonly observed values along similar oceanic transects. Red triangles mark where the plate is ~90, 40, and 10 Ma old.

[47] Regarding the plagioclase-spinel transition, we note that a similar discontinuity has been inferred near a depth of 30 km in the Atlantic, not far from our modeled transect [*Lizarralde et al.*, 2004]. It is tempting at first glance to associate this discontinuity with the plagioclase-spinel phase transition. However, although this hypothesis provides a plausible explanation for the discontinuity, uncertainties in the stability field of spinel precludes a definite conclusion. For instance, it is expected that both plagioclase and spinel coexist within a finite pressure interval in the oceanic lithosphere [*Wood and Yuen*, 1983], which is not modeled well with our present database. A stability field for both phases would reduce the magnitude of the velocity drop at the depth corresponding to the exhaustion of one of the two phases. It follows that our predicted velocity jump ($\Delta Vp \sim 0.1$ km s^{-1}) is

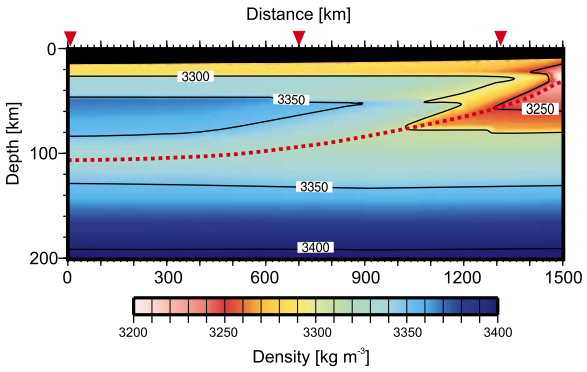

Figure 7. Density structure of the OL and upper sublithospheric mantle down to 200 km depth. Contour lines indicate density in kg m^{-3}. The density jumps due to the plag-spinel (~25 km) and spinel-garnet (~50 km) solid-state phase transitions are evident along the transect. These phase transitions are exothermic, and thus their transition depths deepen toward the ridge (at x = 1500 km). The dotted red line indicates the depth of the 1300°C isotherm. Red triangles mark where the plate is ~90, 40, and 10 Ma old.

likely to be overestimated. In fact, the seismologically derived velocity jump (ΔVp ~ 0.03 km s^{-1}) is 70% smaller than our prediction. Nevertheless, a detectable signature associated with phase transitions in high-Al systems is expected in detailed Vp studies.

[48] Close to the ridge, where the plate is still thin and large temperature gradients exist, the exothermic character of the these phase transitions results in a conspicuous Z-shaped distortion of their equilibrium depths. This is illustrated in Figure 8 with the spinel-garnet transition (yellow dotted lines). The plagioclase-spinel phase transition should behave in a similar fashion, although its Clapeyron slope is more uncertain [*Wood and Yuen*, 1983; *Stixrude and Lithgow-Bertelloni*, 2005a]. The large drop in Vp at ~70 km depth in the 20 Ma model (Figure 9a) is due to the Z-shaped distortion of the spinel-garnet transition, and it would be only present at young ages. In principle, this Vp low is large enough (>2%, Figure 9a) to be detected with Vp studies, but not with shear waves. However, the reduced vertical and lateral extension of this feature may complicate the task. Several seismic transects parallel to a slow spreading ridge (i.e., to avoid complications associated with reaction kinetics) would be necessary to test its existence. Such studies could also provide crucial information on the nature, transition depths, and sharpness of these phase transitions, all of which are important for the stability of oceanic lithosphere. For instance, if the spinel-garnet phase change occurs deep enough to be affected by dynamic processes such as small-scale convection and/or small thermo-chemical plumes, its exothermic nature and associated density change (0.8–1.0% [*Afonso et al.*, 2007]) could favor the thermal erosion of the plate through buoyancy enhancement [cf. *Schubert et al.*, 2001; Zlotnik et al., submitted manuscript, 2008]. On the contrary, if the phase transition occurs well within the highly viscous part of the plate (i.e., shallow depths), its effect on the normal evolution of oceanic lithosphere may become unimportant.

4.3.2. Low-Velocity Zone and Attenuation

[49] A LVZ between ~100 and 200 km depth develops in the oldest parts of the Vs synthetic seismic structure (when attenuation is considered), even though no free melt is included in the computations (Figure 8d). This LVZ, in which absolute velocities and gradients are comparable to those obtained below ocean basins, simply results from the high temperatures and low pressures at these depths. This concurs with recent work [*Faul and Jackson*, 2005; *Stixrude and Lithgow-Bertelloni*, 2005a; *Priestley and McKenzie*, 2006] suggesting that subsolidus processes alone (i.e., anharmonicity and anelasticity) are enough to explain the reduction of seismic velocities at the base of the lithosphere. Since a LVZ at the base of oceanic plates is an invariable feature of our models, which are constrained by other geophysical observables as well, it seems that the concept of the LVZ resulting simply from the effect of temperature on the melt-free solid aggregate is robust. Although there is some evidence that points to the presence of hydrous melts in the LVZ [*Mierdel et al.*, 2007], our results suggest that this cannot be the main cause of velocity reduction (i.e., melt fractions should have to be 0.5%), at least below ocean basins.

[50] An important observation drawn from Figures 8 and 9 is the strong influence that anelastic attenuation has in the final velocity structures, particularly in the Vs case. We find that the inclusion of attenuation at T > 900°C is essential to obtain velocity gradients and magnitudes comparable to those observed in seismic studies (Figures 8d and 9b; compare also Figure 8d with that of *Ritzwoller et al.* [2004]). This also affects the feasibility of identifying compositional heterogeneities in the upper mantle by means of Vp/Vs. For instance, seismological models used to

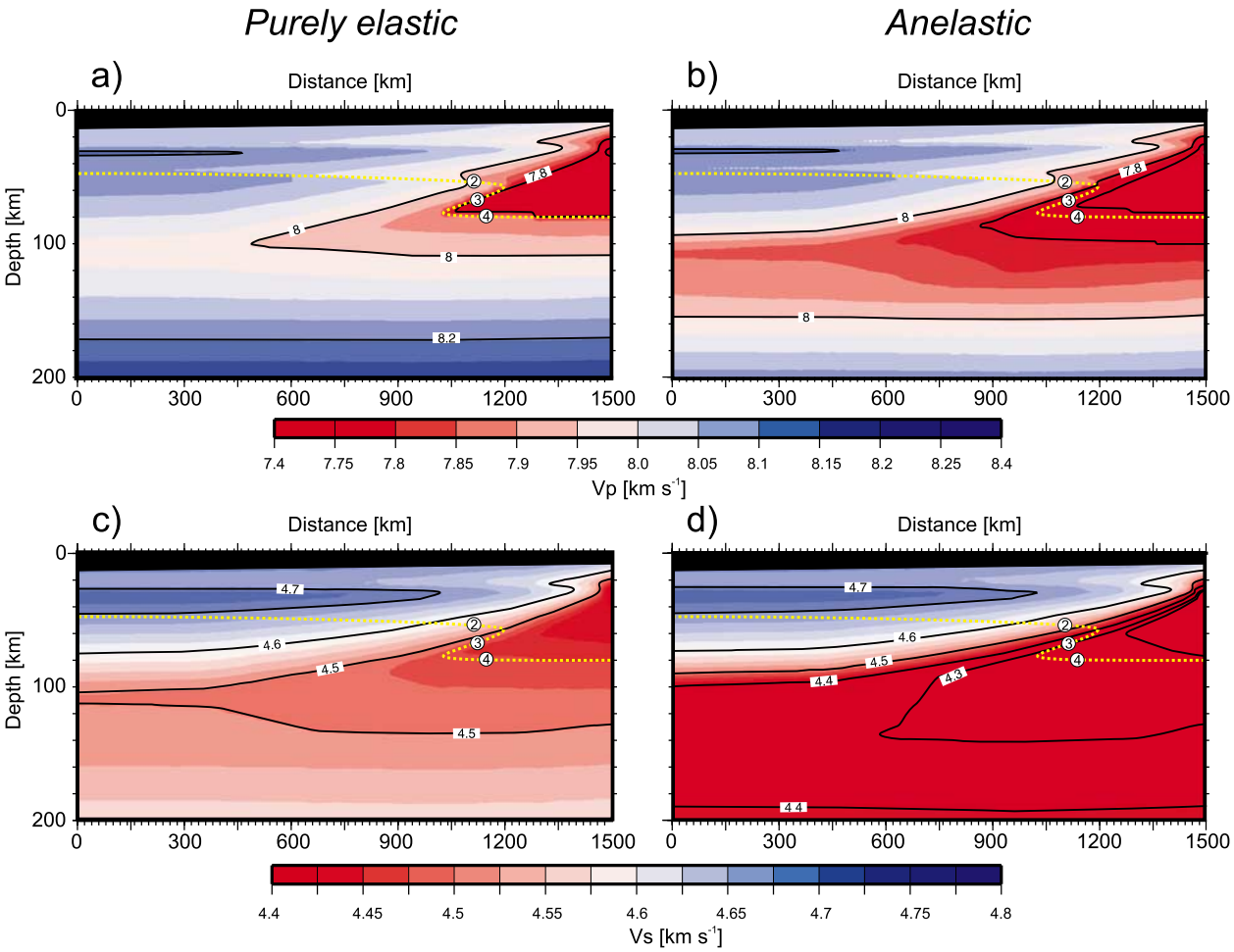

Figure 8. Synthetic Vp (top) and Vs (bottom) seismic structures of the oceanic upper mantle. Contour lines denote seismic velocities in km s^{-1}. Figures 8a and 8c represent results from a purely elastic approximation (no attenuation). Figures 8b and 8d represent results from the anelastic approximation (with attenuation). At the depth range shown the grain size is uniform (d = 3 mm). The activation volume is $V = 1.25 \times 10^{-5}$ m^3 mol^{-1}, and the reference frequency is 25 mHz. The dotted yellow line indicates the approximate location of the spinel-garnet phase transition. Circled numbers denote the multiple spinel-garnet transitions shown in Figure 9. See text for details.

this purpose commonly assume a constant Q throughout the entire studied section. Considering the Vp/Vs resulting from Figures 8b and 8d, the assumption of a constant Q_s of 55 (representative of active regions) results in errors of > + 1 and −1.7% in the retrieved Vp/Vs above and below the 1000°C isotherm, respectively. Similarly, a Q_s of 100 results in errors of >+0.5 and −2.0% above and below the same isotherm. The magnitude of these Vp/Vs variations are comparable to (or larger) those produced by typical compositional changes within the lithospheric mantle (1.4%, own calculation). A complete treatment of this topic is beyond the scope of this paper, but a thorough assessment will be published elsewhere (J. C. Afonso et al., manuscript in preparation, 2008).

[51] Attenuation effects in the above figures were computed as explained in section 3.5 for a uniform grain size d = 3 mm. The activation volume assumed in our computations (1.25×10^{-5} m^3 mol^{-1}) is similar to that given by *Faul and Jackson* [2005] (1.2×10^{-5} m^3 mol^{-1}), which is well within experimental values (closer to the lower limit) given for dislocation creep [*Hirth and Kohlstedt*, 2003]. Our preferred value gives a relatively good fit to the velocity gradients and absolute magnitudes in the quasi-adiabatic part of the mantle. It is also similar to the preferred value reported by *Hirth and Kohlstedt* [2003], and gives a simultaneous fit for Q_s that is roughly consistent with estimates

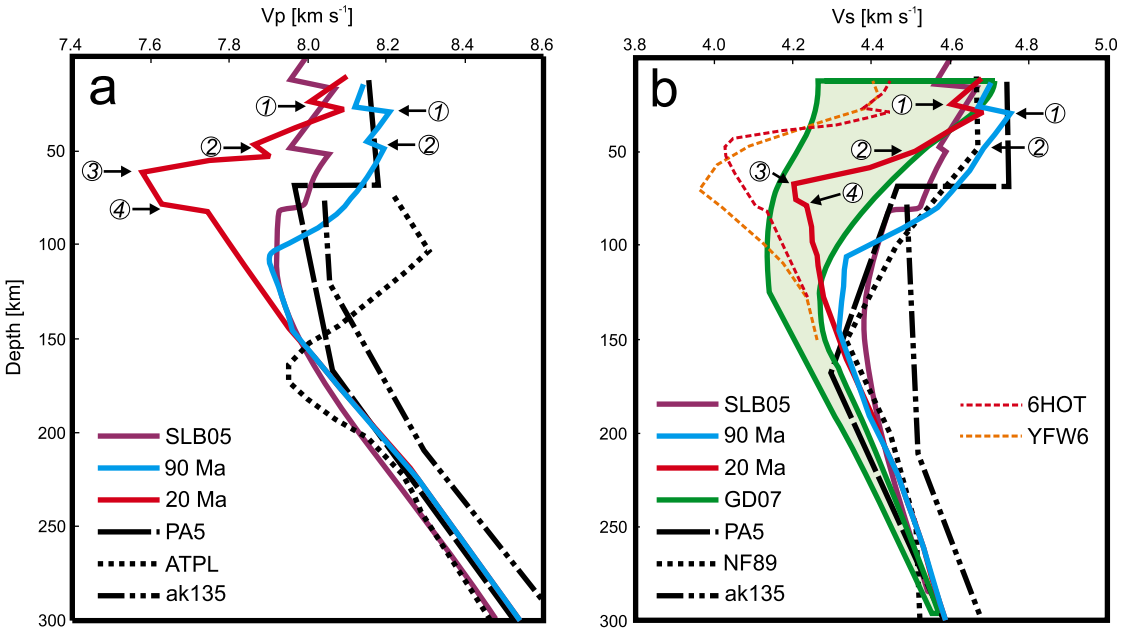

Figure 9. (a) Predicted Vp velocity profiles from our model at ~90 Ma (blue line) and 20 Ma (red line). Both curves include attenuation effects as in Figure 8. Seismological models *ak*135 [*Kennett et al.*, 1995], PA5 [*Gaherty et al.*, 1999], and ATLP [*Zhao and Helmberger*, 1993] are shown for comparison. Both PA5 and ATLP models are representative of OL ~100 Ma old. In the PA5 case we show the average of the horizontal and vertical components. The ATLP is a PH model (PH models are faster than PV models). SLB05 is the mineral physics model of *Stixrude and Lithgow-Bertelloni* [2005a] for OL 100 Ma old (with attenuation). Arrows denote the following phase transitions: 1, plagioclase-spinel; 2, 3, and 4, spinel-garnet. Arrows 3 and 4 correspond to the multiple spinel-garnet transitions shown in Figure 8. (b) Predicted Vs velocity profiles from our model; attenuation, ages, and arrows as in Figure 9a. Seismological models *ak*135, PA5, YFW6, and NF89 [*Nishimura and Forsyth*, 1989] are also shown. The green envelope contains values given by *Gaherty and Dunn* [2007] for OL 15–20 Ma old. YFW6 as in Figure 3c; 6HOT is the "hot" equivalent of our oceanic model for a plate ~6 Ma old in a fast spreading ridge environment (see text).

from seismic studies (Figure 10), although significant differences can be found locally [e.g., *Yang et al.*, 2007]. Unfortunately, experimental uncertainties associated with measurements of V in olivine are still large, and prevent the use of V as a strong constraint on the model.

[52] As a final caveat we note that quantitative comparisons between our synthetic seismic structure in the vicinity of the ridge and those seismically derived in fast spreading ridges (e.g., East Pacific Rise) is not applicable. The oceanic model obtained in this study is based on the fitting of geophysical observables representative of a slow spreading ridge (i.e., Mid-Atlantic ridge). Consequently, model sub-Moho temperatures are low along the entire profile, even when the plate is <10 Ma (Figure 6). Nonetheless, if we increase the temperature close to the ridge to values closer to those estimated in the vicinity of the East Pacific Rise (adiabatic mantle 50°C hotter and sub-Moho temperatures of ~600–700°C [*Dunn et al.*, 2000]), then our predictions become comparable to seismological models (6HOT and YFW6 in Figure 9b). Remaining discrepancies probably can be attributed to differences in depletion and the presence of melt [e.g., *Yang et al.*, 2007].

5. Application to the Cratonic Lithosphere

[53] The Archean SCLM is one of the most well studied lithospheric domains. Three prominent features of Archean cratons are as follows: (1) fast seismic anomalies in the upper 250–350 km depth range [*Ritsema and van Heijst*, 2000; *Gung et al.*, 2003; *Ritsema et al.*, 2004], (2) highly depleted compositions [*Boyd*, 1989; *Boyd et al.*, 1997; *O'Reilly et al.*, 2001; *Griffin and O'Reilly*, 2007], and (3) low SHF [*Pollack et al.*, 1993; *Artemieva and Mooney*, 2001; *Artemieva*, 2006]. These observations are consistent to the first order with a "cratonic tectosphere" model [*Jordan*, 1978], in which Archean domains represent cold, highly depleted residues from multiple partial melting

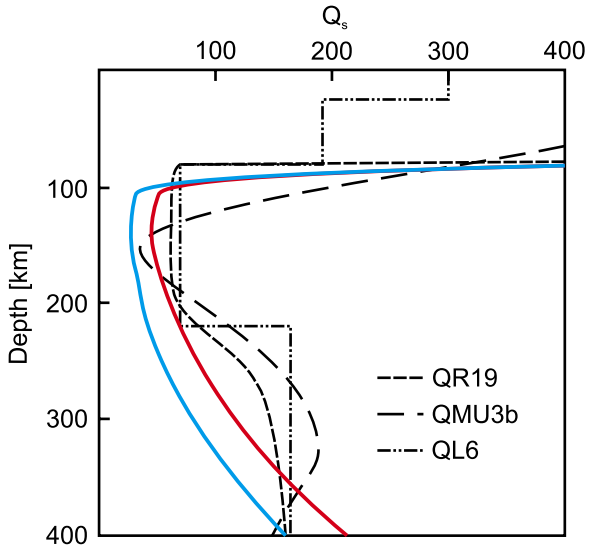

Figure 10. Predictions of shear wave quality factors (Q_s) for ocean basins. Red line is for a case with d = 10 mm and $V = 1.4 \times 10^{-5}$ m^3 mol^{-1}; blue line is for a case with d = 5 mm and $V = 1.2 \times 10^{-5}$ m^3 mol^{-1}. The Q_s trend obtained from our ocean model lies in between these two extremes. Radial models QR19 [*Romanowicz*, 1995], QMU3b [*Selby and Woodhouse*, 2002], and QL6 [*Durek and Ekström*, 1996] are also shown.

events. There are, however, at least two key points that remain controversial with this view. First, the spatial distribution of the high depletion signature observed in mantle samples, and the extent to which metasomatic events modified it, are poorly constrained. The weak correlation between long-wavelength geoid anomalies and cratons suggest that the tectosphere is close to be isopycnic at all depths (i.e., thermal and compositional effects cancel each other out [*Shapiro et al.*, 1999]), but as shown by a number of authors, this condition is hard to reconcile with results from xenolith data, melting experiments, and numerical models [e.g., *Kelly et al.*, 2003; *King*, 2005; *Schutt and Lesher*, 2006]. For instance, typical density differences relative to the convecting mantle from Archean xenoliths (1.5–3%) are usually higher than those required by the isopycnic hypothesis (~1–2%) at depths <160 km [e.g., *Boyd*, 1989; *Boyd et al.*, 1997; *Griffin et al.*, 1999b; *O'Reilly et al.*, 2001; *Mooney and Vidale*, 2003, and references therein]. Second, "representative" compositions for Archean domains as estimated from xenoliths seem to be too buoyant to satisfy isostasy and geoid constraints [e.g., *Mooney and Vidale*, 2003], but too fertile to fit the high seismic velocities observed at depths <80 km in a number of cratons [e.g., *Yliniemia et al.*, 2004; *Deen et al.*, 2006; *Kobussen et al.*, 2006].

[54] *King* [2005] has recently proposed a model for a cratonic keel that attempts to reconcile petrological and geophysical evidence. In this model, the cratonic keel is composed of two boundary layers: (1) a compositional boundary layer, extending to depths of ~175 km, and characterized by being highly depleted with respect to PUM; and (2) a more fertile (but still more depleted than PUM) thermal boundary layer that extends to depths of ~250–300 km, corresponding to the seismological keel inferred from seismic studies [see *King*, 2005, Figure 6]. In principle, this hypothesis should also be compatible with geoid observations, since the positive density anomaly from the thermal boundary layer is offset by the compositional boundary layer above. A somewhat similar vertical stratification can be identified in regions where a large number of mantle samples from different depths is available [e.g., *O'Reilly and Griffin*, 2006] (see below).

[55] Although this keel model seems to be in better agreement with both petrological and geophysical evidence, it has not been quantitatively modeled so far. We perform a series of experiments using synthetic models to address the problems listed above.

5.1. Uniform Models

[56] Figure 11a shows the thermal and compositional structures of the synthetic model and its predictions of SHF, geoid height, and elevation. The model consists of a 3000 km long profile in which a central Archean domain (Archon) is surrounded by "typical" Phanerozoic domains (Tectons). The mantle density distribution of the latter is roughly representative of both mature oceanic and young continental domains. In order to isolate subcrustal effects, we include a homogenous two-layer crust with constant thicknesses of 18 and 21 km, respectively. Its mean radiogenic heat production is set to 0.67 μW m^{-3}, in agreement with estimations for continental crust in Archean domains [*Jaupart and Mareschal*, 2005]. This will bring the calculated SHF in the surrounding Tecton domains closer to the lower end of observations (see below). The elevation is set at 400 m, consistent with the global average for cratons. The compositions assumed for the lithospheric domains correspond to those listed in the first columns of Archons (Aver. Archon Gnt. SCLM) and Tectons (Aver. Tecton Gnt. SCLM)

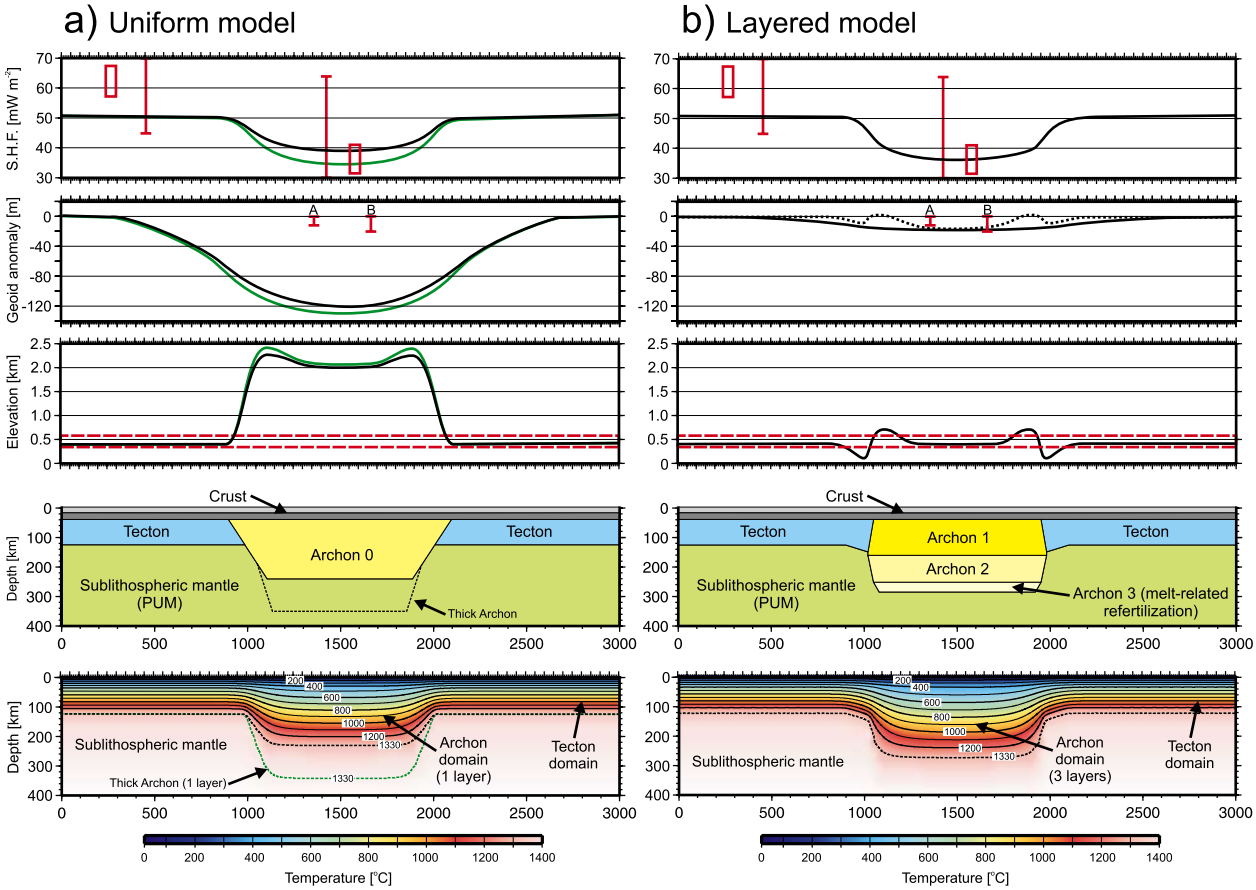

Figure 11. Modeling results of SHF, geoid anomaly, and elevation in Archean domains. The models include a two-layer crustal structure with densities 2765 and 2900 kg m^{-3} (i.e., $\overline{\rho_c} \sim 2835$ kg m^{-3}) in the upper and lower layers, respectively. The geometry and composition of the bodies are shown. Compositions are as follows (refer to Table 1): Tecton, Aver. Tecton Gnt. SCLM; Archon 0, Aver. Archon Gnt. SCLM; Archon 1, Archon "primitive" estimate; Archon 2, Kaapvaal aver. high-T Lherzolite; Archon 3 (refertilized), Aver. Tecton Gnt. SCLM; PUM, PUM MS. The thermal structure is shown in each case in the bottom panels. (a) This model assumes a single composition (Average Archon Gnt. SCLM in Table 1) for the entire SCLM. The thermal structure is depicted in color, and the 1330°C isotherm (black dashed line) denotes the bottom of the lithosphere. Observables predicted by this model are shown with black lines. Also shown are the predictions (green lines) from a similar model, but with a thicker thermal structure (see text). The bottom of the lithosphere is denoted in this case by the green dashed line (1330°C isotherm). (b) Preferred Archean model with three layers of variable composition (depletion). The sinusoidal peaks in elevation and geoid at the borders of the Archean domain are (irrelevant) artifacts due to the sharp lateral transitions assumed between the domains. Solid line in the calculated geoid denotes the 2-D response; the dotted line is the 1-D response. In both Figure s 11a and 11b dashed red lines in elevation represent typical bounds for cratons worldwide. Red bars in geoid represent two estimates of expected geoid signals over shields: A, young continents as reference; B, old oceans as reference [*Shapiro et al.*, 1999]. Red rectangles in SHF are tight estimates for these domains based on regressions of global data (the height of the rectangle denotes possible ranges); red bars indicate the actual variability of the global data [*Artemieva and Mooney*, 2001].

in Table 1, which are commonly assumed as representative averages. The thermal thicknesses are chosen to be consistent with estimates from seismological and thermal studies [e.g., *Artemieva and Mooney*, 2001; *Artemieva*, 2006; *Priestley and McKenzie*, 2006].

[57] For this particular setup, our model predicts elevations (>2 km) and geoid anomalies (>100 m) that are in marked disagreement with observations. This suggests that either the thermal structure or the assumed composition is incorrect. Alternatively, some combination of these effects is also possible.

On the other hand, SHF values lie between commonly observed bounds for Phanerozoic and Archean domains, implying that the thermal structure may be, to the first order, correct. However, since (1) a large part of the SHF in continents is controlled by the distribution of radioactive heat production elements within the crust [*Jaupart and Mareschal*, 2005] and (2) the shallow thermal structure is not particularly sensitive to variations in LAB depth if the latter is located at depths >150–160 km, we anticipate that SHF cannot be taken as a cogent constraint.

[58] To test the model's sensitivity to variations in lithospheric thermal thickness we run an experiment with the same compositions, but increasing the thermal thickness of the Archean domain by 100 km (green dotted line in Figure 11a). Surprisingly, the resulting elevation is slightly higher than in the previous example. This result is at odds with other common methods to calculate absolute elevation of lithospheric sections, which yield a linear relation between the elevation and the thermal thickness of the lithosphere [see, e.g., *Lachenbruch and Morgan*, 1990; *Zeyen and Fernàndez*, 1994]. These models assume that the lithospheric mantle density varies only with temperature and no compositional differences are included. Furthermore, lithospheric columns rest on a fluid asthenosphere with uniform density everywhere (3200 kg m^{-3}). These assumptions force a linear relationship between lithospheric thermal thickness and elevation [*Lachenbruch and Morgan*, 1990], and therefore, the thicker the lithospheric mantle becomes, the greater the subsidence that the column experiences. In contrast, in our model the column reaches isostatic equilibrium at the base of the numerical domain (~410-km discontinuity), and consequently, the sublithospheric mantle (PUM) takes part in the isostatic balance. This implies that when the thermal lithosphere is thinned, two separate and opposite effects take place: (1) the density of the lithospheric mantle is reduced (by thermal expansion), exerting a positive contribution to the elevation; and (2) the average density of the whole column is increased by replacing lithospheric material with PUM (denser) material, exerting a negative contribution to the final elevation. The results in Figure 11a show that, for the assumed Archean composition, these effects almost cancel each other out, although the former is slightly greater. It follows that there is a net (but small) increase in elevation with lithospheric thickening (a similar trend is observed in the geoid anomaly). As envisaged, the SHF does not change significantly (~5 mW m^{-2} after increasing the LAB depth by 100 km).

5.2. Layered Models

[59] It is apparent therefore that the assumed composition is too buoyant (i.e., too depleted) to be representative of the whole section, or its depth distribution is incorrect. However, as discussed above, less depleted compositions are hard to reconcile with both seismic evidence and detailed xenolith studies. There are several possible reasons why published estimates for the composition of Archean SCLM (as those used in our experiment) fail to satisfy the geophysical observables:

[60] 1. Most studies of cratonic xenolith suites have been focused on garnet-bearing peridotites, for which P-T estimates can be made. However, recognition of widespread metasomatic refertilization in peridotite xenoliths and orogenic peridotite massifs [*Simon et al.*, 2004; *Beyer et al.*, 2006; *Griffin and O'Reilly*, 2007, and references therein] suggests that these garnet-bearing samples represent metasomatised rocks, and that primitive Archean SCLM is much more depleted.

[61] 2. Estimates of SCLM composition based on garnet xenocrysts can only sample the less depleted (and probably metasomatised) portions of the deeper SCLM, and can provide no information on the composition of shallower SCLM (depths of 40–90 km). Few analyzed xenoliths provide constraints on this depth range. Estimates of olivine Mg# in the cratonic SCLM [*Griffin et al.*, 2004; *O'Reilly and Griffin*, 2006] commonly show increasing Mg# with decreasing depth, which suggests that shallower SCLM is significantly more depleted than the range sampled by most xenolith/xenocryst suites.

[62] 3. The high opx/olivine ratio of most estimated Archean SCLM compositions is strongly biased toward the composition of peridotite xenoliths from the SW part of the Kaapvaal craton; this is not a representative feature of cratons worldwide. The algorithms of *Griffin et al.* [1999b] for deriving Archean SCLM compositions from garnets also are strongly biased by the Kaapvaal xenolith suite, and thus propagate high opx/olivine ratios to estimates of SCLM composition in other areas.

[63] *Griffin and O'Reilly* [2007] have argued that a more realistic mean composition for the "pristine" Archean SCLM can be based on less metasomatised samples, including the depleted protoliths of

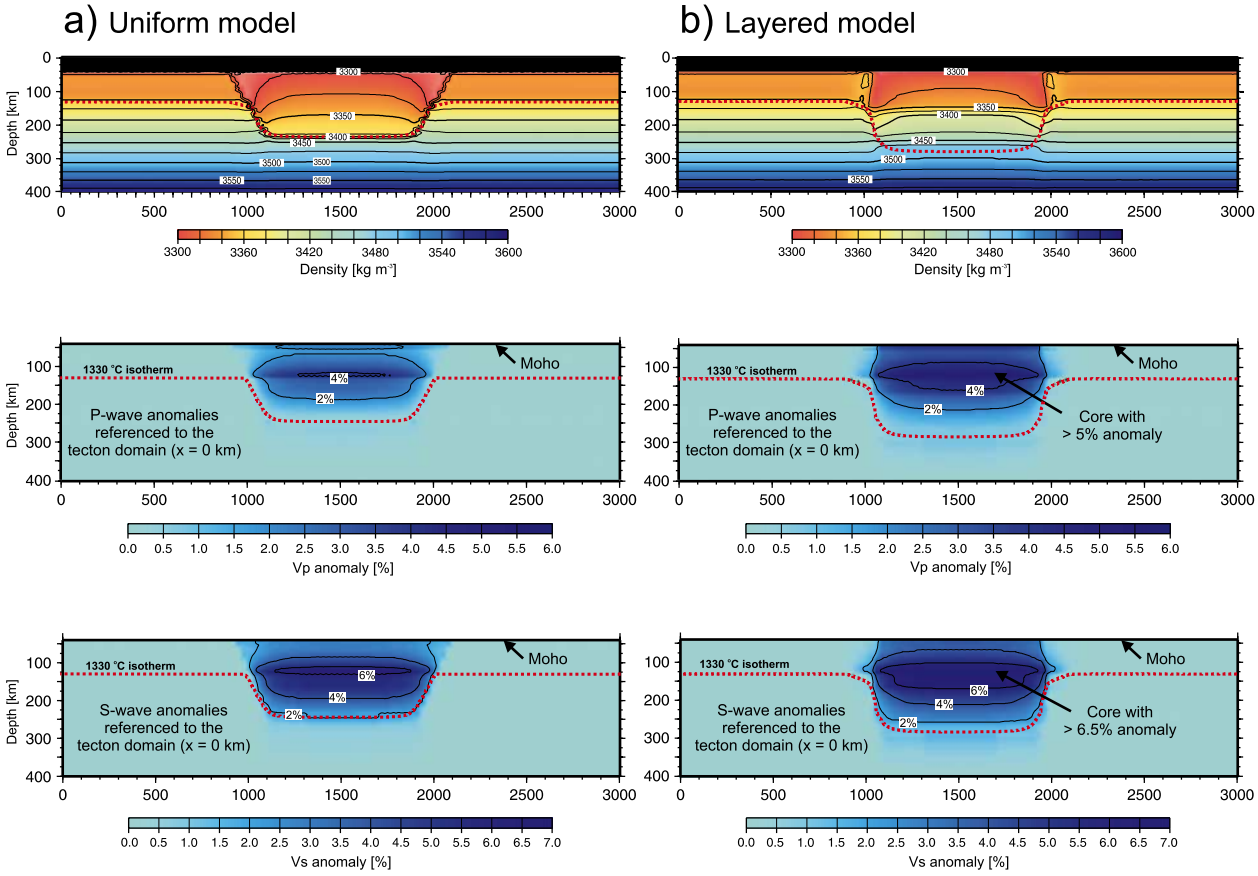

Figure 12. Density structures (kg m^{-3}) and synthetic seismic anomalies (%) for the Archean models shown in Figure 11. The dotted red lines mark the location of the 1330°C isotherm. Seismic anomalies are referenced to a vertical column located at x = 0 km (within the Tecton domain).

peridotite massifs in western Norway [*Beyer et al.*, 2006] and Lherz [*Le Roux et al.*, 2007] and suites of Archean xenoliths from Greenland [*Hanghøj et al.*, 2001]. This estimate (Table 1) is essentially a dunite/harzburgite, with high Mg# and a low opx/olivine ratio.

[64] It therefore seems probable that the typical Archean lithospheric mantle, especially at shallow levels, is more highly depleted than most estimates based on xenolith samples, and that it becomes more fertile with depth. On the basis of this hypothesis, we tested different vertical stratifications that would be compatible with both geophysical and petrological evidence. Figure 11b shows one of our preferred models and its predictions of SHF, elevation, and geoid anomaly. Its density structure and predicted velocity anomalies are shown in Figure 12. The model includes (1) a highly depleted (dunitic/harzburgitic) layer that extends from the Moho to a depth of 160 km, (2) a less depleted (refertilized?) layer extending from 160 to 250 km depth, and (3) a compositional buffer layer extending from 250 to 280 km depth with a composition only slightly more depleted than the underlying PUM. The first layer represents the "pristine" most depleted layer as estimated from xenoliths and peridotite massifs [*Griffin and O'Reilly*, 2007, Table 1]. In detail, according to estimates of olivine Mg# in SCLM, the composition of this upper layer is also expected to vary with depth (see above). The intermediate layer represents a more fertile domain, yet more depleted than the PUM, consistent with observations from the Kaapvaal and Slave cratons [e.g., *Boyd et al.*, 1999; *Griffin et al.*, 1999a]. The lowermost layer attempts to mimic a melt-related metasomatised layer [see, e.g., *O'Reilly and Griffin*, 2006, and references therein] at the bottom of the lithosphere (LAB).

[65] Predictions from this keel model (and other similar examples not shown here) are in good agreement with observables in cratons worldwide.

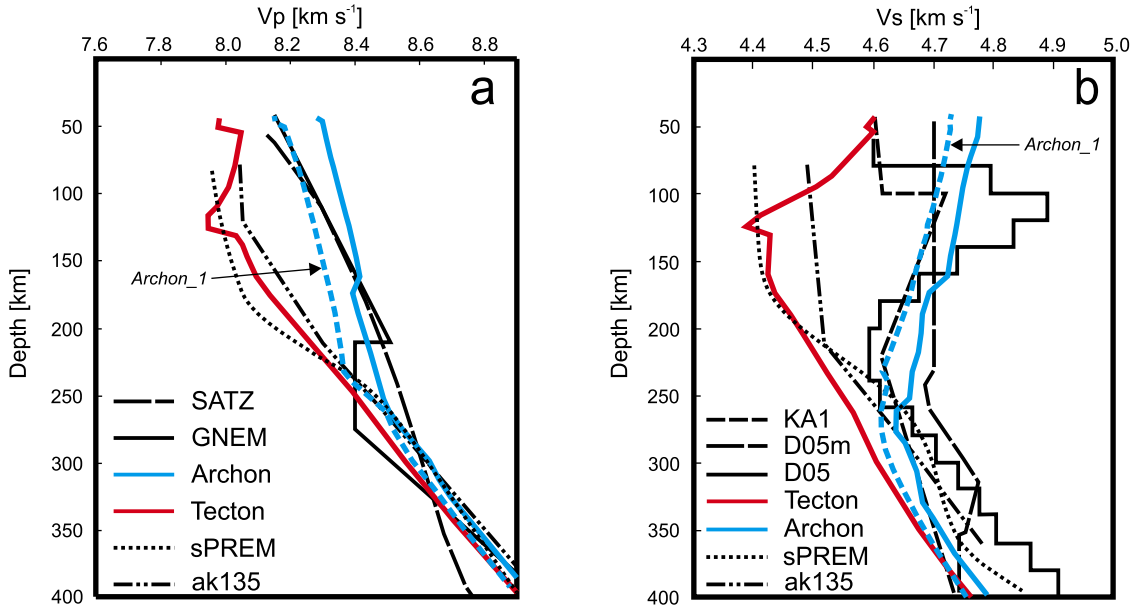

Figure 13. (a) Predicted Vp velocity profiles from the modeled Tecton (red line) and Archon (blue line) domains. Both curves include attenuation effects as follows: d = 1 cm, $V = 1.3 \times 10^{-5}$ m^3 mol^{-1}, T_o = 50 s. Seismological models in cratonic areas SATZ [*Zhao et al.*, 1999] and GNEM [*Ryberg et al.*, 1997] are shown for comparison. Global models "smooth" PREM (sPREM) and *ak*135 are also shown. (b) Predicted Vs velocity profiles from the same model. Seismological models in cratonic areas KA1 [*Freybourger et al.*, 2001] and D05-D05m (FRB-YMBN from *Darbyshire* [2005]) are shown for comparison. The dashed blue lines (Archon_1) are predictions from the uniform Archon model (Figures 11 and 12). Attenuation effects as in Figure 13a.

Absolute elevations vary between 350 and 550 m, well within the global average. Geoid anomalies (relative to the off-craton domains) are ~−20 m, comparable to those estimated by *Shapiro et al.* [1999] over platforms and shields. Predicted SHF values are also in agreement with reported measurements in cratons [*Jaupart and Mareschal*, 2005; *Artemieva*, 2006]. Seismic velocity anomalies shown in Figure 12 resemble very closely those from tomography studies below cratons, particularly for the cases of the Siberian craton, Baltic shield, and Canadian shield [*Ritsema and van Heijst*, 2000; *Röhm et al.*, 2000; *Ritsema et al.*, 2004]. Interestingly, Vp and Vs velocities at 50–80 km depth reach values of 8.30–8.35 and 4.78–4.75 km s^{-1} (Figure 13), consistent with the high velocities measured in these regions, but still significantly lower than those recorded in the Fennoscandian shield and the Siberian craton (>8.7–8.8 km s^{-1} [*Yliniemia et al.*, 2004; *Kobussen et al.*, 2006]). Although anisotropy is likely to be an important effect in these regions, cross-cutting profiles suggest that these velocities have a significant isotropic component. Introducing shallow and thin layers with dunitic compositions (olivine Mg# ~94–94.5) in our models yields isotropic Pn velocities of the order of 8.5 km s^{-1}, without shifting the observables outside the expected limits. However, reaching isotropic Vp values of 8.7 km s^{-1} requires temperatures far too low for being realistic. We conclude that cold dunitic rocks alone cannot explain the anomalously high velocities recorded in the Fennoscandian shield and the Siberian craton. Either an anisotropic signal of at least 3.5% or the presence of eclogitic material at shallow depths is necessary to fit the observed velocities.

[66] Another illustration of the added-value of our method follows from a comparison of the velocity profiles shown in Figure 13. It can be seen that the shapes of the Vp and Vs profiles predicted by the uniform and layered models are almost identical, suggesting that the compositional stratification would not be recoverable by seismic methods alone. Moreover, using typical (anharmonic) temperature derivatives from the literature (∂Vp/∂T ~−0.00044 km s^{-1} °C^{-1}; ∂Vs/∂T ~−0.00033 km s^{-1} °C^{-1} [*Goes et al.*, 2000; *Lee*, 2003]), the predicted difference in absolute velocities between these two models at depths <140 km (i.e., where anelasticity is unimportant) would require temperature differences of 150–200°C, while the real ΔT

in this case is only 100°C (Figure 11). It follows that compositional differences can affect temperature estimations from seismic studies by as much as 100°C.

[67] Although beyond the scope of this paper, we note that a LVZ is somewhat apparent in the Archean when considering the high velocities of the shallow lithosphere and deep sublithospheric mantle (Figure 13b). The decrease in Vs with depth is 2.3% in the first 200 km, reaching ~3.0% at 280 km depth. The Vp profile, however, shows a monotonous increase in velocity with depth (Figure 13a). The Vs velocity distribution depicted in Figure 13b is comparable to those obtained in seismological studies in some stable areas [see *Thybo*, 2006, and references therein], which raises the question of the importance of melts and/or fluids for generating a detectable LVZ in continental areas.

[68] Finally, we note that in the case of Archean domains, more than 40% of the lithospheric mantle has temperatures >900°C (refer to Figure 11), and therefore any attempt to identify possible compositional variations from seismic studies must include a reliable attenuation model.

6. Conclusions

[69] We have presented a combined and self-consistent geophysical-petrological methodology to study the thermal, compositional, density, and seismological structure of the lithospheric-sublithospheric upper mantle. The methodology has been incorporated into a finite-element code (LitMod) that allows the generation of integrated 2-D forward models from the surface down to the 410-km discontinuity. Different geophysical observables (i.e., gravity anomalies, surface heat flow, geoid height, elevation, and seismic velocities) are simultaneously fitted, thus reducing the uncertainties associated with the modeling of these observables alone or in pairs, as typically done in geophysical modeling. This provides a better control on possible compositional and thermal fields, since these observables are differentially sensitive to the spatial distribution of these fields.

[70] We have applied this methodology to both oceanic and continental lithospheric domains. Our results can be summarized as follows:

[71] 1. Mature oceanic plates with thermal thicknesses of 105 ± 5 km are consistent with available geophysical and petrological data. The existence of phase transitions within oceanic plates depends on its major-element compositional structure, and therefore on the petrological processes occurring at the MOR. Detailed Vp studies could provide information on their nature and transition depths, which carry important implications for the evolution and stability of the oceanic lithosphere.

[72] 2. The development of a subsolidus LVZ between ~100–200 km depth is an invariable feature of our oceanic models, which are constrained by other geophysical and petrological observables as well. No free melt effects are needed to reproduce the absolute velocities and gradients observed in ocean basins, suggesting that the main cause for the velocity reduction in the LVZ beneath oceans is of thermal origin.

[73] 3. The strong temperature dependence of anelastic attenuation in mantle aggregates at temperatures >900–1000°C and uncertainties in both experimental parameters and thermal fields make the identification of compositional variations in the lower lithospheric-sublithospheric mantle unreliable when using seismic data only (e.g., from Vp/Vs ratios). More experimental data and integrated modeling techniques are needed to provide reliable constraints on compositional heterogeneities.

[74] 4. Modeling of a typical Archean craton and its surrounding Tecton domains shows that accepted mantle compositions and thermal structures for Tectons are compatible with geophysical observables. However, successful modeling of the Archon block requires a lithospheric keel that differs in structure and composition from commonly accepted models based on xenolith suites. Geophysical and petrological observations can be explained by a keel model that consists of a highly depleted dunite/harzburgite (Mg# > 93; low opx/olivine) to depths of ca 160 km, underlain by more fertile (approximately isopycnic) compositions down to ca 280–300 km.

Appendix A

A1. Density of Silicate Melts

[75] The density of silicate melts as a function of pressure, temperature, and composition can be obtained in a way similar to that used in section 3.2 for solid phases [e.g., *Lange and Charmichael*, 1987; *Cella and Rapolla*, 1997]. The method presented by *Lange and Charmichael* [1987] is adopted here. In this model, the isothermal bulk

modulus of the silicate melt K_T depends on melt composition and compressibility as

$$K_T = \frac{1}{\sum X_i \, \beta_{i,T}} \tag{A1}$$

where X_i is the mole fraction of the constituent oxides and $\beta_{i,T}$ is the isothermal compressibility of the respective oxides at a given T. $\beta_{i,T}$ is obtained from

$$\beta_{i,T} = \beta_{i,Tr} + \frac{d\beta_{i,Tr}}{dT}(T - Tr) \tag{A2}$$

where Tr is a reference temperature. Experimental values for all relevant parameters (including molar volumes from which $\rho_{0(T,\,0)}$ is obtained) and their temperature derivatives are taken from *Lange and Charmichael* [1987]. In lieu of reliable experimental results, we assume here $K_{0(T,\,0)}{}' = 4$ for silicate melts. The density of the melt is calculated substituting the above parameters in equation (3).

A2. Total Amount of Partial Melting

[76] Partial melting experiments on natural mantle peridotites have provided important constraints on the total amount of partial melting that can be produced at certain P-T conditions [cf. *Kushiro*, 2001]. Together with formal thermodynamic relations, this information can be used to constraint the total amount of partial melting necessary to generate a "standard" oceanic crust ~6–7 km thick [e.g., *Klein and Langmuir*, 1987; *McKenzie and Bickle*, 1988; *Asimow et al.*, 2001, 2004; *Kushiro*, 2001; *Presnall et al.*, 2002]. *Klein and Langmuir* [1987] were among the first to define a formalism for the relationship between F and the thickness of oceanic crust, h_c, at the ridge. Defining the pressure of intersection of the solidus as P_o and the pressure at which melting stops as P_f, then the total amount of melt F present within a unit column is

$$F = \int_{P_0}^{P_f} F(P) \quad dP \tag{A3}$$

The mean fraction of melting $\overline{F}$ is

$$\overline{F} = \frac{\int_{P_0}^{P_f} F(P) \quad dP}{(P_\circ - P_f)} \tag{A4}$$

In general, the function $F(P)$ will be a complex function of P (depth). However, it can always be approximated, within a finite pressure interval n, with a constant slope $\gamma_n = (dF/dP)_S$ (the productivity function [*Langmuir et al.*, 1992; *Phipps Morgan*, 2001]) given by

$$\left(\frac{dF}{dP}\right)_S = \frac{\frac{\alpha T}{\rho c_p} - \left(\frac{\partial T_s}{\partial P}\right)_F}{\frac{H_m}{c_p} + \left(\frac{\partial T_s}{\partial F}\right)_P} \tag{A5}$$

where T_s is the solidus temperature, α the CTE, c_p the heat capacity, and H_m the heat of fusion (or latent heat of melting). For commonly accepted values of these variables, average γ values range between 10 and 20% per GPa of pressure release [see, e.g., *Langmuir et al.*, 1992]. The amount of melt present at any pressure P_x is given by the sum of γ_n $(P_{n-1} - P_n)$ for all relevant n, where P_n becomes P_x in the last pressure interval and P_{n-1} is P_o in the first pressure interval. Equation (A3) thus becomes

$$F = \int_{P_0}^{P_f} \sum_{n=1}^{n} \gamma_n (P_{n-1} - P_n) \quad dP \tag{A6}$$

or, using equation (A4)

$$F = \overline{F}(P_\circ - P_f) \tag{A7}$$

Note that in equation (A6) the productivity function γ has units of P^{-1} (i.e., melt produced per unit of pressure release). Thus, F is given in units of P (e.g., GPa). Assuming that the total amount of melt produced in each increment of spreading is segregated to form the oceanic crust, then equations (A3) and (A6) give the crustal thickness h_c (strictly, the weight of a melt column of height h_c [*Klein and Langmuir*, 1987; *Langmuir et al.*, 1992]) as

$$\rho_c g h_c = \overline{F}(P_\circ - P_f) \tag{A8}$$

Taking pressure in GPa, densities in kg m^{-3}, and $\overline{F}$ in %, a good approximation of h_c in km is

$$h_c = \overline{F}(P_\circ - P_f)\frac{10^4}{\rho_c g} \tag{A9}$$

For example, for typical values of [*Asimow et al.*, 1999, 2001] $\overline{F}$ ~7.2%, P_o ~2.75 GPa, P_f ~ 0.2 GPa, and ρ_c = 2880 kg m^{-3}, equation (A9) gives $h_c \sim 6.5$ km.

[77] Hence, values of $\overline{F}$ > than about 10% (F > 25%) are considered to be inconsistent with the

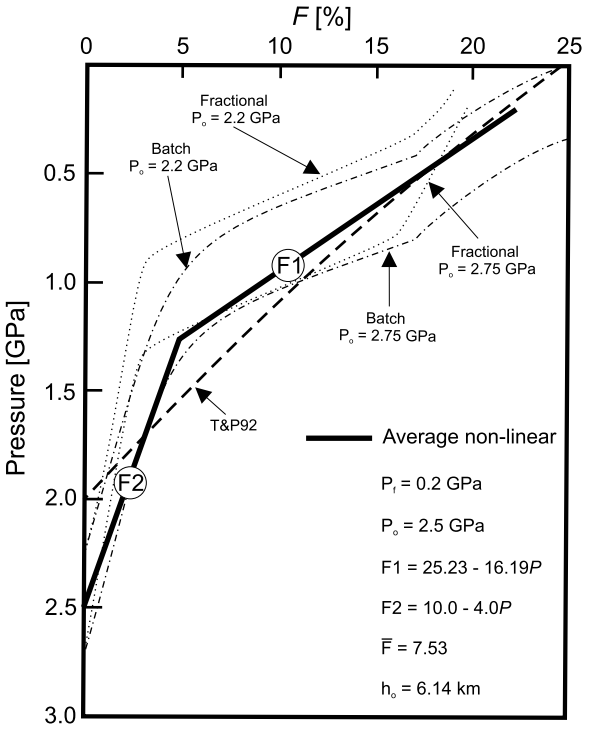

Figure A1. Degree of partial melting with depth for different melting models. The two dotted and two dash-dotted curves are isentropic melting models for fractional melting and batch melting at two different P_o, respectively [from *Asimow et al.*, 1999, 2001]. The dashed line is the model of *Turcotte and Phipps Morgan* [1992]. The solid line is our preferred model. F1 and F2 are two linear functions used in the numerical implementation of the average nonlinear model. Pressure in these functions is in GPa. Other relevant parameters are listed in the right bottom corner.

normal amount of crust produced, except of course at sites of active upwellings, where the crust can reach anomalous thicknesses. Figure A1 shows a summary of the results presented by *Asimow et al.* [1999, 2001] for both batch and fractional melting models. The widely used quasi-linear model (i.e., with constant γ, hereafter QL) is also included in Figure A1 [*Langmuir et al.*, 1992; *Turcotte and Phipps Morgan*, 1992]. The preferred nonlinear model used in this work is shown with solid bold lines. It corresponds to a peridotite solidus with approximately 180–190 ppm H_2O in the source [*Hirth and Kohlstedt*, 1996; *Asimow et al.*, 2004]. It is important to note here that, although the form of γ might vary from one work to another, the product of $(P_o - P_f)$ and $\overline{F}$ should be comparable in all cases.

A3. Depth Distribution of Melt

[78] Due to the high compressibility of melts, significant amounts of melt within a MOR column can affect its final average density to a considerable extent. For example, 22% partial melting at 10 km would reduce the density of mantle material by ~3.4% (including chemical depletion of the solid phase), while the same amount of partial melting at 80 km would only reduce the density by ~1.8%. Fortunately, both theoretical and experimental considerations indicate that the actual amount of melt retained within a MOR column (i.e., porosity) is small [*Spiegelman and Kelemen*, 2003], making its effect on density changes less important. Since the form of the melt productivity function affects both the porosity and the composition of the solid residue, the melting model in Figure A1 can be used as a proxy for modeling the actual melt distribution with depth. The actual amount and depth distribution of the retained melt beneath a MOR are still under debate, but trace-element and U-series disequilibrium modeling indicate maximum retained melt fractions of ~1% [e.g., *Spiegelman and Kelemen*, 2003, and references therein]. In accordance with these studies, a maximum retained melt fraction of 1% is assumed here at the top of the mantle column, and is varied linearly with depth until it reaches a value of 0.5% at the point where γ experiences a drastic slope change (at 1.25 GPa). Below this point the melt fraction decreases linearly again until the bottom of the melting regime, where it becomes zero.

A4. Chemical Variation of Both Solid and Melt Phases Due to Partial Melting

[79] The final chemical composition of a solid-liquid system is basically determined by three parameters: the initial concentration of the element or component in the system °C, the bulk distribution coefficient D, and the fraction of liquid F. To a first-order approximation, the composition of the solid residue can be estimated as [*Langmuir et al.*, 1992]

$$x_i^s = \frac{x_i^o}{F/D_i + (1-F)} \tag{A10}$$

where x_i^o is the concentration of the ith oxide in the original source (in wt %) and D_i is its bulk partition coefficient. The composition of the melt is of less importance here because its final density does not

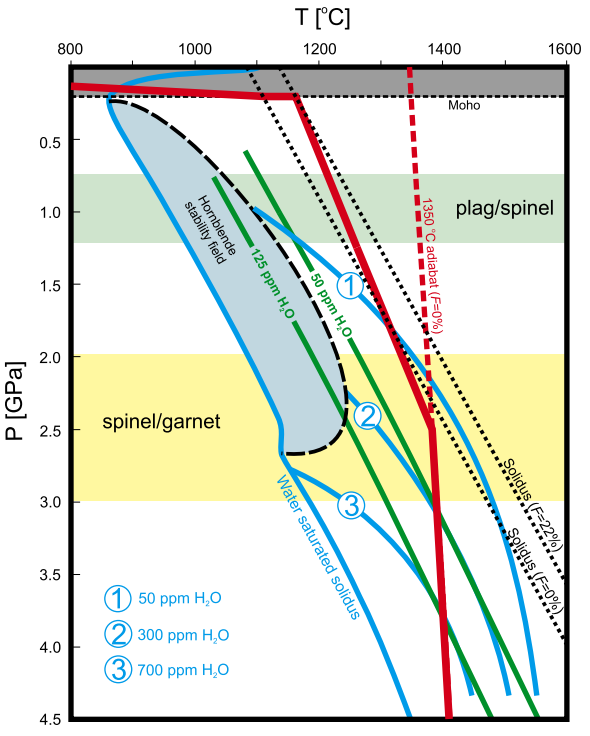

Figure A2. Modeled geotherm beneath a MOR (solid red) and mantle adiabat (dashed red) for a basal temperature of 1520°C at 400 km depth. Black dotted lines represent two mantle solidus with no melting and after 22% melt extraction. Blue lines are wet solidus for different amounts of water from *Asimow et al.* [2004]. Green lines are the same as blue lines but from *Hirth and Kohlstedt* [1996]. The transition depths for the two relevant solid-state phase transitions and their associated uncertainty are also shown.

change dramatically for a normal range of MORB compositions (both accumulated fractional and batch melting result in similar melt compositions [*Langmuir et al.*, 1992]). Here is estimated from a simple mass balance constraint as

$$x_i^l = x_i^s / D_i \tag{A11}$$

Empirical partition coefficients $D_i(F,P)$ adequate for a MOR environment are taken from *Niu* [1997]. Although it is acknowledged that this simple model is not appropriate for modeling trace element systematics or detailed MORB compositions, differences with more sophisticated models in terms of residual modal compositions and melt densities are unimportant.

A5. Solid-State Phase Transitions and Temperature Gradient

[80] The temperature distribution with depth below a MOR is calculated with [cf. *Phipps Morgan*, 2001]

$$\left(\frac{dT}{dP}\right)_{MOR} = \left(\frac{dT_s}{dP}\right)_F - \left(\frac{dT_s}{dF}\right)_P \left\{ \frac{\left(\frac{\partial T_s}{\partial P}\right)_F - \frac{\alpha T}{\rho c_p}}{\frac{H_m}{c_p} + \left(\frac{\partial T_s}{\partial F}\right)_P} \right\} \tag{A12}$$

assuming a basal temperature of 1520°C at 400 km depth. In regions where there is no partial melting ($H_m = 0$), equation (A12) becomes the common expression for the mantle adiabatic gradient ($\alpha T/\rho c_p$). The variation of the coefficient of thermal expansion with P, T, and composition is also included in our computations following *Afonso et al.* [2005]. Parameters used to solve equation (A12) are as follows [*Phipps Morgan*, 2001]: $(dT_s/dP)_F$ = 130°C GPa^{-1}; $(dT_s/dF)_P$ = 250°C; c_p = 1200 J kg^{-1}°C^{-1}; H_m/c_p = 550°C.

[81] The plagioclase-spinel and spinel-garnet phase transitions reduce the temperature of a mantle parcel ascending beneath a MOR. However, as *Phipps Morgan* [2001] pointed out, this effect is very minor (~5–10°C) and can be ignored in our calculation.

[82] The combined effects of shallow hydrothermal circulation and conductive cooling in the first 10 km depth are subject to larger (and unquantifiable) uncertainties and thus they are not explicitly modeled. Instead, they are simulated by adjusting the temperature gradient in this region to give a final SHF of 250–300 mW m^{-2}. Figure A2 shows the final temperature profile beneath a MOR together with solidus estimations for various water contents in the source.

Appendix B

[83] There is no perfect compensation level in the Earth's mantle; temperature and pressure disturbances associated with convective flow prevent its existence. However, it can be shown that in a mantle-like fluid, surface topography is primarily controlled by temperature (density) variations in the vicinity of the upper thermal boundary layer (i.e., lithosphere) and is relatively insensitive to thermal (density) anomalies below a certain critical isotherm [*Parsons and Daly*, 1983]. This critical isotherm, which should coincide roughly with the

isotherm that defines the base of the lithosphere, seems to separate two domains. The upper domain is viscous enough to support internal loads, either thermal or compositional, over geologic timescales. In other words, large horizontal pressure gradients can exist within this domain and its internal density distribution will dominate the topographic signature. The lower domain, on the other hand, is less viscous, and even small pressure gradients tend to be relaxed rapidly through fluid flow (e.g., small-scale convection). If the dynamic effect of flow on surface topography is neglected (a second-order effect over distances of a few 1000 km, except over large plumes or downwellings [*Parsons and Daly*, 1983; *Marquart and Schmeling*, 1989; *Lithgow-Bertelloni and Silver*, 1998]), then the compensation level can be put at any depth below the critical isotherm. In our isostatic balance, the thermal gradient in the sublithospheric mantle does not include thermal perturbations that could arise from convection, which means that dynamic loads are implicitly ignored.

[84] Besides the isobaric condition used in our isostatic balance, it is also desirable for modeling purposes that temperature does not vary significantly along the compensation level. In this context, since lateral pressure variations within the Earth's mantle are thought to be small, the topography of discontinuities provides information on lateral variations in temperature. In principle, if the discontinuities are produced by phase changes, smooth topographies should correspond to small temperature contrasts. Global seismic studies have revealed variations of up to ±20–30 km in the topography of the 410-km mantle discontinuity [e.g., *Flanagan and Shearer*, 1999; *Chambers et al.*, 2005, and references therein]. These figures decrease to ∼50% at more regional scales (1500 km) [*Fee and Dueker*, 2004; *Chambers et al.*, 2005; *Suetsugu et al.*, 2007]. Using a Clapeyron slope of +4.0 MPa K^{-1} for the $\alpha-$ to β-olivine (wadsleyite) phase change [*Katsura et al.*, 2004], regional variations in temperature along the transition zone should be restricted to values ±125 K, even close to hotspots and some subduction zones [*Fee and Dueker*, 2004; *Suetsugu et al.*, 2007]. However, these estimates need to be taken with caution. As [*Chambers et al.*, 2005] and [*Katsura et al.*, 2004] pointed out, it is not clear as to what extent compositional and temperature variations combine to produce the observed topography of the 410-km discontinuity at short wavelengths. Since our model assumes a constant composition (PUM) in the sublithospheric mantle, as well as an adiabatic gradient, modeling results are strictly valid where long-wavelength dynamic effects and/or short-wavelength lithospheric loads are absent (see above). However, if these effects can be estimated by other means (e.g., seismic tomography), they can be used to correct the input/outputs of LitMod [*Afonso*, 2006].

Acknowledgments

[85] Many colleagues provided stimulating discussions and valuable comments on the topics presented in this paper. Special thanks go to S. O'Reilly, S. Goes, Z. Tašárová, M. Schimmel, J. Gallart, N. Simon, D. Brown, and R. Carbonell. We also thank J. Fullea for helping with some numerical implementations and J. Jackson for helpful comments and references on the anomalous behavior of orthoenstatite. This manuscript was significantly improved by thoughtful reviews by S. Goes, J. Gaherty, and an anonymous reviewer. This work was supported by the Spanish research projects 01-LEC-EMA22F-EUROMARGINS-ESF, CTM2005-08071-C03-03/MAR, and Consolider TopoIberia CSD2006-00041 (J.C.A. and M.F.), NSERC (Natural Sciences and Engineering Research Council of Canada) grants (G.R.), and ARC and Macquarie University grants (W.L.G.). This is contribution 521 from the ARC National Key Centre for Geochemical Evolution and Metallogeny of Continents.

References

Afonso, J. C. (2006), Thermal, density, seismological, and rheological structure of the lithospheric-sublithospheric mantle from combined petrological-geophysical modelling: Insights on lithospheric stability and the initiation of subduction, Ph.D. thesis, Carleton Univ., Ottawa, Ontario, Canada. (Available at http://wija.ija.csic.es/gt/afonso/homepage.htm)

Afonso, J. C., G. Ranalli, and M. Fernàndez (2005), Thermal expansivity and elastic properties of the lithospheric mantle: Results from mineral physics of composites, *Phys. Earth Planet. Inter.*, *149*, 279–306.

Afonso, J. C., G. Ranalli, and M. Fernàndez (2007), Density structure and buoyancy of the oceanic lithosphere revisited, *Geophys. Res. Lett.*, *34*, L10302, doi:10.1029/2007GL029515.

Angel, R. J. (2000), Equations of state, in *High-Temperature and High-Pressure Crystal Chemistry, Rev. Mineral. Geochem.*, vol. 41, edited by R. M. Hazen and R. T. Downs, pp. 935–959, Mineral. Soc. of Am., Washington, D. C.

Angel, R. J. (2004), Equations of state of plagioclase feldspars, *Contrib. Mineral. Petrol.*, *146*, 506–512.

Artemieva, I. (2006), Global $1^{\circ} \times 1^{\circ}$ thermal model TC1 for the continental lithosphere: Implications for lithosphere secular evolution, *Tectonophysics*, *416*, 245–277.

Artemieva, I., and W. Mooney (2001), Thermal thickness and evolution of Precambrian lithosphere: A global study, *J. Geophys. Res.*, *106*, 16,387–16,414.

Artemieva, I., M. Billien, J. Lèvêque, and W. Mooney (2004), Shear wave velocity, seismic attenuation, and thermal structure of the continental upper mantle, *Geophys. J. Int.*, *157*, 607–628.

Asimow, P. D., M. M. Hirschmann, and E. M. Stolper (1999), An analysis of variations in isentropic melt productivity, in *Mid-Ocean Ridges: Dynamics of Processes Associated With Creation of New Ocean Crust*, edited by J. R. Cann, H. Elderfield, and A. Laughton, pp. 39–65, Cambridge Univ. Press, New York.

Asimow, P. D., M. M. Hirschmann, and L. M. Stolper (2001), Calculation of peridotite partial melting form thermodynamic model of minerals and melts, IV. Adiabatic decompression and the composition and mean properties of mid-ocean basalts, *J. Petrol.*, *42*, 963–998.

Asimow, P. D., J. E. Dixon, and C. H. Langmuir (2004), A hydrous melting and fractionation model for mid-ocean ridge basalts: Application to the Mid-Atlantic Ridge near the Azores, *Geochem. Geophys. Geosyst.*, *5*, Q01E16, doi:10.1029/2003GC000568.

Baker, M., and E. M. Stolper (1994), Determining the composition of high-pressure mantle melts using diamond aggregates, *Geochim. Cosmochim. Acta*, *58*(13), 2811–2827.

Beyer, E., W. Griffin, and S. O'Reilly (2006), Transformation of Archean lithospheric mantle by refertilization: Evidence from exposed peridotites in the Western Gneiss Region, Norway, *J. Petrol.*, *47*, 1611–1636.

Boyd, F. R. (1989), Compositional distinction between oceanic and cratonic lithosphere, *Earth Planet. Sci. Lett.*, *96*, 15–26.

Boyd, F. R., N. P. Pokhilenko, D. G. Pearson, S. A. Mertzman, N. V. Sobolev, and L. W. Finger (1997), Composition of the Siberian cratonic mantle: Evidence from Udachnaya peridotite xenoliths, *Contrib. Mineral Petrol.*, *128*, 228–246.

Boyd, F. R., D. G. Pearson, and S. A. Mertzman (1999), Spinel-facies peridotites from the Kaapvaal root, in *Proceedings of the VII International Kimberlite Conference*, edited by J. J. Gurney et al., pp. 40–48, Red Roof Design, Cape Town, South Africa.

Brey, G. P., A. M. Doroshev, A. V. Girnis, and A. I. Turkin (1999), Garnet-spinel-olivine-orthopyroxene equilibria in the FeO-MgO-Al_2O_3-SiO_2-Cr_2o_3 system: I. Composition and molar volumes of minerals, *Eur. J. Mineral.*, *11*, 599–617.

Cammarano, F., S. Goes, P. Vacher, and D. Giardini (2003), Inferring upper mantle temperatures from seismic velocities, *Phys. Earth Planet. Inter.*, *138*, 197–222.

Cella, F., and A. Rapolla (1997), Density changes in upwelling mantle, *Phys. Earth Planet. Inter.*, *103*, 63–84.

Chambers, K., J. H. Woodhouse, and A. Deuss (2005), Topography of the 410-km discontinuity from PP and SS precursors, *Earth Planet. Sci. Lett.*, *235*, 610–622.

Connolly, J. A. D. (2005), Computation of phase equilibria by linear programming: A tool for geodynamic modeling and its application to subduction zone decarbonation, *Earth Planet. Sci. Lett.*, *236*, 524–541.

Connolly, J. A. D., and D. M. Kerrick (2002), Metamorphic controls on seismic velocity of subducted oceanic crust at 100–250 km depth, *Earth Planet. Sci. Lett.*, *204*, 61–74.

Darbyshire, F. (2005), Upper mantle structure of Arctic Canada from Rayleigh wave dispersion, *Tectonophysics*, *405*, 1–23.

Deen, T. J., W. L. Griffin, G. Begg, S. Y. O'Reilly, L. M. Natapov, and J. Hronsky (2006), Thermal and compositional structure of the subcontinental lithospheric mantle: Derivation from shear wave seismic tomography, *Geochem. Geophys. Geosyst.*, *7*, Q07003, doi:10.1029/2005GC001120.

Dunn, R. A., and D. W. Forsyth (2003), Imaging the transition between the region of mantle melt generation and the crustal magma chamber beneath the southern East Pacific Rise with short-period Love waves, *J. Geophys. Res.*, *108*(B7), 2352, doi:10.1029/2002JB002217.

Dunn, R., D. R. Toomey, and S. C. Solomon (2000), Three-dimensional seismic structure and physical properties of the crust and shallow mantle beneath the East Pacific rise at 9°30′N, *J. Geophys. Res.*, *105*, 23,537–23,555.

Durek, J. J., and G. Ekström (1996), A radial model of anelasticity consistent with long-period surface-wave attenuation, *Bull. Seismol. Soc. Am.*, *86*, 144–158.

Dziewonski, A. M., and D. L. Anderson (1981), Preliminary Reference Earth Model, *Phys. Earth Planet. Inter.*, *25*, 297–356.

Ebbing, J., C. Braitenberg, and H. J. Götze (2006), The lithospheric Density structure of the Eastern Alps, *Tectonophysics*, *414*, 145–155.

Faul, U. H., and I. Jackson (2005), The seismological signature of temperature and grain size variations in the upper mantle, *Earth Planet. Sci. Lett.*, *234*, 119–134.

Fee, D., and K. Dueker (2004), Mantle transition zone topography and structure beneath the Yellowstone hotspot, *Geophys. Res. Lett.*, *31*, L18603, doi:10.1029/2004GL020636.

Fei, Y. (1995), Thermal expansion, in *Mineral Physics and Crystallography: A Handbook of Physical Constants*, *AGU Ref. Shelf*, vol. 2, edited by T. J. Ahrens, pp. 283–291, AGU, Washington, D. C.

Fei, Y., and C. M. Berkta (1999), Phase transitions in the Earth's mantle and mantle mineralogy, in *Mantle Petrology: Field Observations and High-Pressure Experimentation: A Tribute to Francis R. (Joe) Boyd*, edited by Y. Fei, C. M. Berkta, and B. O. Mysen, *Spec Publ. Geochem. Soc.*, *6*, 189–207.

Flanagan, M. P., and P. M. Shearer (1999), A map of topography on the 410-km discontinuity from PP precursors, *Geophys. Res. Lett.*, *26*, 549–552.

Flesch, L. M., B. Li, and R. C. Liebermann (1998), Sound velocities of Polycrystalline $MgSiO_3$ orthopyroxene to 10 GPa at room temperature, *Am. Mineral.*, *83*, 444–450.

Freybourger, M., J. Gaherty, and T. Jordan (2001), Structure of the Kaapvaal craton from surface waves, *Geophys. Res. Lett.*, *28*, 2489–2492.

Frost, D. J. (2003), The structure and sharpness of $(Mg,Fe)_2SiO_4$ phase transformations in the transition zone, *Earth Planet. Sci. Lett.*, *216*, 313–328.

Fullea, J., M. Fernàndez, H. Zeyen, and J. Vergés (2007), A rapid method to map the crustal and lithospheric thickness using elevation, geoid anomaly and thermal analysis: Application to the Gibraltar Arc System, Atlas Mountains and adjacent zones, *Tectonophysics*, *430*, 97–117.

Gaherty, J. B., and R. A. Dunn (2007), Evaluating hot spot–ridge interaction in the Atlantic from regional-scale seismic observations, *Geochem. Geophys. Geosyst.*, *8*, Q05006, doi:10.1029/2006GC001533.

Gaherty, J. B., M. Kato, and T. H. Jordan (1999), Seismological structure of the upper mantle: A regional comparison of seismic layering, *Phys. Earth Planet. Inter.*, *110*, 21–41.

Goes, S., R. Govers, and P. Vacher (2000), Shallow mantle temperatures under Europe from P and S wave tomography, *J. Geophys. Res.*, *105*, 11,153–11,169.

Green, D., and A. Ringwood (1970), Mineralogy of peridotitic compositions under upper mantle conditions, *Phys. Earth Planet. Inter.*, *3*, 359–371.

Green, D. H., and T. J. Falloon (1998), Pyrolite: A Ringwood concept and its current expression, in *The Earth's Mantle: Composition, Structure and Evolution*, edited by I. Jackson, pp. 311–378, Cambridge Univ. Press, New York.

Griffin, W. L., and S. Y. O'Reilly (2007), The earliest subcontinental lithospheric mantle, in *Earth's Oldest Rocks, Dev. Precambrian Geol*, vol. 15, edited by M. van Kranendonk,

H. Smithies, and V. Bennett, chap. 39, pp. 1013–1036, Elsevier, New York.

Griffin, W. L., A. Zhang, S. O'Reilly, and C. Ryan (1998), Phanerozoic evolution of the lithosphere beneath the Sino-Korean Craton, in *Mantle Dynamics and Plate Interactions in East Asia, Geodyn. Ser.*, vol. 27, edited by M. Flower et al., pp. 107–126, AGU, Washington, D. C.

Griffin, W. L., B. Doyle, C. Ryan, N. Pearson, S. O'Reilly, R. Davies, K. Kivi, E. Van Achterbergh, and L. Natapov (1999a), Layered mantle lithosphere in the Lac de Gras Area, Slave Craton: Composition, structure and origin, *J. Petrol.*, *40*, 705–727.

Griffin, W. L., S. Y. O'Reilly, and C. G. Ryan (1999b), The composition and origin of sub-continental lithospheric mantle, in *Mantle Petrology: Field Observations and High-Pressure Experimentation: A Tribute to Francis R. (Joe) Boyd*, edited by Y. Fei, C. M. Berkta, and B. O. Mysen, *Spec. Publ. Geochem. Soc.*, 6, 13–45.

Griffin, W. L., C. G. Ryan, F. V. Kaminsky, S. Y. O'Reilly, L. M. Natapov, T. Win, P. D. Kinny, and I. P. Ilupin (1999c), The Siberian lithosphere traverse: Mantle terranes and the assembly of the Siberian Craton, *Tectonophysics*, *310*, 1–35.

Griffin, W. L., Z. V. Spetsius, N. J. Pearson, and S. Y. O'Reilly (2002), In situ Re-Os analysis of sulfide inclusions in kimberlitic olivine: New constraints on depletion events in the Siberian lithospheric mantle, *Geochem. Geophys. Geosyst.*, *3*(11), 1069, doi:10.1029/2001GC000287.

Griffin, W. L., S. O'Reilly, B. Doyle, N. Pearson, K. Kivi, V. Malkovets, H. Coopersmith, and N. Pokhilenko (2004), Lithosphere mapping beneath the North American plate, *Lithos*, *77*, 873–922.

Gu, Y. J., S. C. Webb, and J. B. Gaherty (2005), Upper mantle structure beneath the eastern Pacific Ocean ridges, *J. Geophys. Res.*, *110*, B06305, doi:10.1029/2004JB003381.

Gung, Y., M. Panning, and B. Romanowicz (2003), Global anisotropy and the thickness of continents, *Nature*, *422*, 707–711.

Gwanmesia, G. D., J. Zhang, K. Darling, J. Kung, B. Li, L. Wang, D. Neuville, and R. C. Liebermann (2006), Elasticity of polycrystalline pyrope ($Mg_3Al_2Si_3O1_2$) to 9 GPa and 1000 °C, *Phys. Earth Planet. Int.*, *155*, 179–190.

Hammond, W. C., and E. D. Humphreys (2000), Upper mantle seismic wave velocity: Effects of realistic partial melt geometries, *J. Geophys. Res.*, *105*, 10,975–10,986.

Hanghøj, K., P. Kelemen, S. Bernstein, J. Blusztajn, and R. Frei (2001), Osmium isotopes in the Wiedemann Fjord mantle xenoliths: A unique record of cratonic mantle formation by melt depletion in the Archaean, *Geochem. Geophys. Geosyst.*, *2*(1), doi:10.1029/2000GC000085.

Hashin, Z., and S. Shtrikman (1963), A variational approach to the theory of the elastic behaviour of multiphase minerals, *J. Mech. Phys. Solids*, *11*, 127–140.

Hasterok, D., and D. S. Chapman (2007), Continental thermal isostasy: 1. Methods and sensitivity, *J. Geophys. Res.*, *112*, B06414, doi:10.1029/2006JB004663.

Hill, R. (1952), The elastic behavior of a crystalline aggregate, *Proc. R. Soc. London, Ser. A*, *65*, 349–354.

Hirth, G., and D. L. Kohlstedt (1996), Water in the oceanic upper mantle: Implications for rheology, melt extraction and the evolution of the lithosphere, *Earth Planet. Sci. Lett.*, *144*, 93–108.

Hirth, G., and D. L. Kohlstedt (2003), Rheology of the upper mantle and the Mantle wedge: A view from the experimentalists, in *Inside the Subduction Factory, Geophys. Monogr. Ser.*, vol. 138, edited by J. Eiler, pp. 83–105, AGU, Washington, D. C.

Hofmeister, A. M. (1999), Mantle values of thermal conductivity and the geotherm from phonon lifetimes, *Science*, *283*, 1699–1706.

Huang, J., and S. Zhong (2005), Sublithospheric small-scale convection and its implications for the residual topography at old ocean basins and the plate model, *J. Geophys. Res.*, *110*, B05404, doi:10.1029/2004JB003153.

Isaak, D. G., I. Ohno, and P. C. Lee (2006), The elastic constants of monoclinic single-crystal chrome-diopside to 1300 K, *Phys. Chem. Miner.*, *32*, 691–699.

Ito, E., and T. Katsura (1989), A temperature profile of the mantle transition zone, *Geophys. Res. Lett.*, *16*, 425–428.

Jackson, I., J. D. Fitz Gerald, U. H. Faul, and B. H. Tan (2002), Grain-size-sensitive seismic wave attenuation in polycrystalline olivine, *J. Geophys. Res.*, *107*(B12), 2360, doi:10.1029/2001JB001225.

Jackson, J. M., S. V. Sinogeikin, and J. D. Bass (2007), Sound velocities and single-crystal elasticity of orthoenstatite to 1073 K at ambient pressure, *Phys. Earth Planet. Inter.*, *161*, 1–12.

Jagoutz, E., H. Palme, H. Baddenhausen, K. Blum, M. Cendales, G. Dreibus, B. Spettel, V. Lorenz, and H. Wanke (1979), The abundance of major, minor and trace elements in the Earth's mantle as derived from primitive ultramafic nodules, *Proc. Lunar Planet. Sci. Conf. 10th*, 2031–2050.

Jaupart, C., and J. C. Mareschal (2005), Constraints on crustal heat production from heat flow data, in *Treatise on Geochemistry*, vol. 3, *The Crust*, edited by R. L. Rudnick, H. D. Holland, and K. K. Turekian, pp. 65–84, Elsevier, New York.

Ji, S., Q. Wang, and B. Xia (2003), P-wave velocities of polymineralic rocks: Comparison of theory and experiment and test of elastic mixture rules, *Tectonophysics*, *366*, 165–185.

Jordan, T. H. (1978), Composition and development of the continental tectosphere, *Nature*, *274*, 544–548.

Karato, S. I. (1993), Importance of anelasticity in the interpretation of seismic tomography, *Geophys. Res. Lett.*, *20*, 1623–1626.

Karato, S. (2003), Mapping water content in the upper mantle, in *Inside the Subduction Factory*, *Geophys. Monogr. Ser.*, vol. 138, edited by J. Eiler, pp. 135–152, AGU, Washington, D. C.

Katsura, T., et al. (2004), Olivine-wadsleyite transition in the system $(Mg,Fe)_2SiO_4$, *J. Geophys. Res.*, *109*, B02209, doi:10.1029/2003JB002438.

Kelly, R. K., P. B. Kelemen, and M. Jull (2003), Buoyancy of the continental upper mantle, *Geochem. Geophys. Geosyst.*, *4*(2), 1017, doi:10.1029/2002GC000399.

Kennett, B. L. N., E. R. Engdahl, and R. Buland (1995), Constraints on seismic velocities in the Earth from traveltimes, *Geophys. J. Int.*, *122*, 108–124.

King, S. D. (2005), Archean cratons and mantle dynamics, *Earth Planet. Sci. Lett.*, *234*, 1–14.

Klein, E. M., and C. H. Langmuir (1987), Global correlations of ocean ridge basalt chemistry with axial depth and crustal thickness, *J. Geophys. Res.*, *92*, 8089–8115.

Klemme, S. (2004), The influence of Cr on the garnet-spinel transition in the Earth's mantle: Experiments in the system MgO-Cr_2O_3-SiO_2 and thermodynamic modelling, *Lithos*, *77*, 639–646.

Klemme, S., and H. S. O'Neill (1998), The partitioning of chromium between orthopyroxene and spinel in the system MgO-Al_2O_3-SiO_2-Cr_2O_3, *Mineral. Mag.*, *62A*, 789–790.

Kobussen, A., N. I. Christensen, and H. Thybo (2006), Constraints on seismic velocity anomalies beneath the Siberian craton from xenoliths and petrophysics, *Tectonophysics*, *425*, 123–135.

Kukkonen, I., and R. Lahtinen (2001), Variation of radiogenic heat production rate in 2.8-1.8 Ga old rocks in the central Fennoscandian shield, *Phys. Earth Planet. Inter.*, *126*, 279–294.

Kung, J., B. Li, T. Uchida, Y. Wang, D. Neuville, and R. C. Liebermann (2004), In-situ measurements of sound velocities and densities across the orthopyroxene - high-pressure clinopyroxene transition in $MgSiO_3$ at high pressure, *Phys. Earth Planet. Inter.*, *147*, 27–44.

Kung, J., B. Li, T. Uchida, and Y. Wang (2005), In-situ elasticity measurement for the unquenchable high-pressure clinopyroxene phase: Implication for the upper mantle, *Geophys. Res. Lett.*, *32*, L01307, doi:10.1029/2004GL021661.

Kushiro, I. (2001), Partial melting experiments on peridotite and origin of mid-ocean ridge basalt, *Annu. Rev. Earth Planet. Sci.*, *29*, 71–107.

Lachenbruch, A. H., and P. Morgan (1990), Continental extension, magmatism, and elevation: Formal relations and rules of thumb, *Tectonophysics*, *174*, 39–62.

Lange, R., and I. Charmichael (1987), Densities of Na_2O, K_2O, CaO, MgO, FeO, Fe_2O_3, Al_2O_3, TiO_2, SiO_2 liquids: New measurements and derived partial molar properties, *Geochim. Cosmochim. Acta*, *51*(11), 2931–2946.

Langmuir, C. H., E. M. Klein, and T. Plank (1992), Petrological systematics of mid-ocean ridge basalts: Constraints on melt generation beneath ocean ridges, in *Mantle Flow and Melt Generation at Mid-Ocean Ridges*, *Geophys. Monogr. Ser.*, vol. 71, edited by J. Phipps Morgan, D. K. Blackman, and J. M. Sinton, pp. 183–280, AGU, Washington, D. C.

Le Roux, V., J. Bodinier, A. Tommasi, O. Alard, J. Dautria, A. Vauchez, and A. Riches (2007), The Lherz spinel lherzolite: Refertilized rather than pristine mantle, *Earth Planet. Sci. Lett.*, *259*, 599–612.

Lee, C. A. (2003), Compositional variation of density and seismic velocities in natural peridotites at STP conditions: Implications for seismic imaging of compositional heterogeneities in the upper mantle, *J. Geophys. Res.*, *108*(B9), 2441, doi:10.1029/2003JB002413.

Lemoine, F., et al. (1998), The Development of the Joint NASA GSFC and NIMA Geopotential Model EGM96, *NASA/TP-1998-206861*, NASA Goddard Space Flight Cent., Greenbelt, Md.

Lesher, C., and M. B. Baker (1997), Near-solidus phase relations of a mantle peridotite at 3.6–5 GPa, *Eos Trans. AGU*, *78*(46), 812.

Lithgow-Bertelloni, C., and P. G. Silver (1998), Dynamic topography, plate driving forces, and the African superswell, *Nature*, *395*, 269–272.

Lizarralde, D., J. B. Gaherty, J. A. Collins, G. Hirth, and S. D. Kim (2004), Spreading-rate dependence of melt extraction at mid-ocean ridges from mantle seismic refraction data, *Nature*, *432*, 744–747.

Marquart, G., and H. Schmeling (1989), Topography and geoid undulations caused by small-scale convection beneath continental lithosphere of variable elastic thickness, *Geophys. J.*, *97*, 511–527.

Matsukage, K. N., Y. Nishihara, and S. Karato (2005), Seismological signature of chemical differentiation of Earth's upper mantle, *J. Geophys. Res.*, *110*, B12305, doi:10.1029/2004JB003504.

McDonough, W. F., and S. Sun (1995), The composition of the Earth, *Chem. Geol.*, *120*, 223–253.

McKenzie, D., and M. J. Bickle (1988), The volume and composition of melt generated by extension of the lithosphere, *J. Petrol.*, *29*, 625–679.

McKenzie, D., J. Jackson, and K. Priestley (2005), Thermal structure of oceanic and continental lithosphere, *Earth Planet. Sci. Lett.*, *233*, 337–349.

Michael, P., and E. Bonatti (1985), Peridotite composition from the North Atlantic: Regional and tectonic variations and implications for partial melting, *Earth Planet. Sci. Lett.*, *73*, 91–104.

Mierdel, K., H. Keppler, J. Smyth, and F. Langenhorst (2007), Water solubility in aluminous orhtopyroxene and the origin of the Earth's asthenosphere, *Science*, *315*, 364–368.

Mooney, W. D., and J. E. Vidale (2003), Thermal and chemical variations in Subcrustal cratonic lithosphere: Evidence from crustal isostasy, *Lithos*, *71*, 185–193.

Mueller, R., W. Roest, J. Royer, L. M. Gahagan, and J. G. Sclater (1997), Digital isochrons of the world's ocean floor, *J. Geophys. Res.*, *102*, 3211–3214.

National Geophysical Data Center (2001), 2-minute Gridded Global Relief Data (ETOPO2), technical report, Natl. Oceanic and Atmos. Admin., U.S. Dept. of Commer., Washington, D. C.

Nishimura, C., and D. Forsyth (1989), The anisotropic structure of the upper mantle in the Pacific, *Geophys. J.*, *96*, 203–229.

Niu, Y. (1997), Mantle melting and melt extraction processes beneath ocean ridges: Evidence from abyssal peridotites, *J. Petrol.*, *38*, 1047–1074.

Niu, Y. (1999), Comments on some missconceptions in igneous and experimental petrology and methodology: A reply, *J. Petrol.*, *40*, 1195–1203.

Niu, Y. (2004), Bulk-rock major and trace element compositions of abyssal peridotites: Implications for mantle melting, melt extraction and post-melting processes beneath mid-ocean ridges, *J. Petrol.*, *45*, 2423–2458.

Niu, Y., C. H. Langmuir, and R. J. Kinzler (1997), The origin of abyssal peridotites: A new perspective, *Earth Planet. Sci. Lett.*, *152*, 251–265.

O'Reilly, S. Y., and W. L. Griffin (2006), Imaging global chemical and thermal heterogeneity in the subcontinental lithospheric mantle with garnets and xenoliths: Geophysical implications, *Tectonophysics*, *416*, 289–309.

O'Reilly, S. Y., W. L. Griffin, Y. H. Poudjom Djomani, and P. Morgan (2001), Are lithospheres forever? Tracking changes in subcontinental lithospheric mantle through time, *GSA Today*, *11*, 4–10.

Palme, H., and H. S. O'Neill (2005), Cosmochemical estimates of mantle composition, in *Treatise on Geochemistry*, vol. 2, *The Mantle and Core*, edited by R. W. Carlson, H. D. Holland, and K. K. Turekian, pp. 1–38, Elsevier, New York.

Parsons, B., and S. Daly (1983), The relationship between surface topography, gravity anomalies, and temperature structure of convection, *J. Geophys. Res.*, *88*, 1129–1144.

Pavese, A., V. Diella, V. Pischedda, M. Meril, R. Bocchio, and M. Mezouar (2001), Pressure-volume-temperature equation of state of andradite and grossular, by high-pressure and -temperature powder diffraction, *Phys. Chem. Miner.*, *28*, 242–248.

Pearson, D. G., G. J. Irvine, R. W. Carlson, M. G. Kopylova, and D. A. Ionov (2002), The development of lithospheric keels beneath the earliest continents: Time constraints using

PGE and Re-Os isotope systematics, in *The Early Earth: Physical, Chemical and Biological Development*, edited by C. M. R. Fowler, C. J. Ebinger, and C. J. Hawkesworth, *Geol. Soc. Spec. Publ.*, *199*, 65–90.

Phipps Morgan, J. (2001), Thermodynamics of pressure release melting of a veined plum pudding mantle, *Geochem. Geophys. Geosyst.*, *2*(4), doi:10.1029/2000GC000049.

Poirier, J. (2000), *Introduction to the Physics of the Earth's Interior*, 2nd ed., Cambridge Univ. Press, Cambridge, U. K.

Pollack, H. N., S. J. Hurter, and J. R. Johnson (1993), Heat flow from the Earth's interior: Analysis of the global data set, *Rev. Geophys.*, *31*, 267–280.

Poudjom-Djomani, Y. H., S. Y. O'Reilly, W. L. Griffin, and P. Morgan (2001), The density structure of subcontinental lithosphere through time, *Earth Planet. Sci. Lett.*, *184*, 605–621.

Presnall, D. C., G. H. Gudfinnsson, and M. J. Walter (2002), Generation of mid-ocean ridge basalts at pressures from 1 to 7 GPa, *Geochim. Cosmochim. Acta*, *66*, 2073–2090.

Priestley, K., and D. McKenzie (2006), The thermal structure of the lithosphere from shear wave velocities, *Earth Planet. Sci. Lett.*, *244*, 285–301.

Ritsema, J., and H. van Heijst (2000), New seismic model of the upper mantle beneath Africa, *Geology*, *28*, 63–66.

Ritsema, J., H. J. van Heijst, and J. H. Woodhouse (2004), Global transition zone tomography, *J. Geophys. Res.*, *109*, B02302, doi:10.1029/2003JB002610.

Ritzwoller, M. H., N. M. Shapiro, and S. J. Zhong (2004), Cooling history of the Pacific lithosphere, *Earth Planet. Sci. Lett.*, *226*, 69–84.

Röhm, A., R. Snieder, S. Goes, and J. Trampert (2000), Thermal structure of continental upper mantle inferred from S-wave velocity and surface heat flow, *Earth Planet. Sci. Lett.*, *181*, 395–407.

Romanowicz, B. (1995), A global tomographic model of shear attenuation in the upper mantle, *J. Geophys. Res.*, *100*, 12,375–12,394.

Ryberg, T., F. Wenzel, A. Egorkin, and L. Solodilov (1997), Properties of the mantle transition zone in northern Eurasia, *J. Geophys. Res.*, *103*, 811–822.

Sandwell, D. T., and H. W. F. Smith (1997), Marine gravity anomalies from GEOSAT and ERS-1 satellite altimetry, *J. Geophys. Res.*, *102*, 10,039–10,054.

Schubert, G., D. L. Turcotte, and P. Olson (2001), *Mantle Convection in the Earth and Planets*, 940 pp., Cambridge Univ. Press, U. K.

Schutt, D. L., and C. E. Lesher (2006), Effects of melt depletion on the density and seismic velocity of garnet and spinel lherzolite, *J. Geophys. Res.*, *111*, B05401, doi:10.1029/2003JB002950.

Selby, N. D., and J. H. Woodhouse (2002), The Q structure of the upper mantle: Constraints from Rayleigh wave amplitudes, *J. Geophys. Res.*, *107*(B5), 2097, doi:10.1029/2001JB000257.

Shahnas, M. H., and R. N. Pysklywec (2004), Anomalous topography in the western Atlantic caused by edge-driven convection, *Geophys. Res. Lett.*, *31*, L18611, doi:10.1029/2004GL020882.

Shapiro, S. S., B. H. Hager, and T. H. Jordan (1999), The continental tectosphere and Earth's long-wavelength gravity field, *Lithos*, *48*, 135–152.

Shinmei, T., N. Tomioka, K. Fujino, K. Kuroda, and T. Irifune (1999), In-situ x-ray diffraction study of enstatite up to 12 GPa and 1473 K and equation of state, *Am. Mineral.*, *84*, 1588–1594.

Shirey, S., J. Harris, S. Richardson, M. Fouch, D. James, P. Cartigny, P. Deines, and F. Viljoen (2002), Diamond genesis, seismic structure, and evolution of the Kaapvaal-Zimbabwe Craton, *Science*, *297*, 1683–1686.

Simon, N., G. Irvine, G. Davies, D. Pearson, and R. Carlson (2004), The origin of garnet and clinopyroxene in "depleted" kaapvaal peridotites, *Lithos*, *71*, 289–322.

Simon, N., E.-R. Newmann, C. Bonadiman, M. Coltorti, G. Delpech, and M. Gregorie (2008), Ultra-refractory domains in the oceanic mantle lithosphere sampled as mantle xenoliths at ocean islands, *J. Petrol.*, in press.

Sobolev, S. V., H. Zeyen, G. Stoll, F. Werling, R. Altherr, and K. Fuchs (1996), Upper mantle temperatures from teleseismic tomography of French Massif Central including effects of composition, mineral reactions, anharmonicity, anelasticity and partial melt, *Earth Planet. Sci. Lett.*, *139*, 147–163.

Speziale, S., T. S. Duffy, and R. J. Angel (2004), Single-crystal elasticity of fayalite to 12 GPa, *J. Geophys. Res.*, *109*, B12202, doi:10.1029/2004JB003162.

Spiegelman, M., and P. B. Kelemen (2003), Extreme chemical variability as a consequence of channelized melt transport, *Geochem. Geophys. Geosyst.*, *4*(7), 1055, doi:10.1029/2002GC000336.

Stein, C. A., and S. Stein (1992), A model for the global variation in oceanic depth and heat flow with lithospheric age, *Nature*, *359*, 123–128.

Steinberger, B., H. Schmeling, and G. Marquart (2001), Large-scale lithospheric stress field and topography induced by global mantle convection, *Earth Planet. Sci. Lett.*, *186*, 75–91.

Stixrude, L., and M. S. T. Bukowinski (1990), Fundamental thermodynamic relations and silicate melting with implications for the constitution of d", *J. Geophys. Res.*, *95*, 19,311–19,325.

Stixrude, L., and C. Lithgow-Bertelloni (2005a), Mineralogy and elasticity of the oceanic upper mantle: Origin of the low-velocity zone, *J. Geophys. Res.*, *110*, B03204, doi:10.1029/2004JB002965.

Stixrude, L., and C. Lithgow-Bertelloni (2005b), Thermodynamics of mantle Minerals—1: Physical properties, *Geophys. J. Int.*, *162*, 610–632.

Suetsugu, D., H. Shiobara, H. Sugioka, Y. Fukao, and T. Kanazawa (2007), Topography of the mantle discontinuities beneath the South Pacific superswell as inferred from broadband waveforms on seafloor, *Phys. Earth Planet. Inter.*, *160*, 310–318.

Suzuki, A., E. Ohtani, and T. Kato (1998), Density and thermal expansion of a peridotite melt at high pressure, *Phys. Earth Planet. Inter.*, *107*, 53–61.

Talwani, M., J. Worzel, and L. Landisman (1959), Rapid computations for two-dimensional bodies with application to the Mendocino submarine fracture zone, *J. Geophys. Res.*, *64*, 49–59.

Thybo, H. (2006), The heterogeneous upper mantle low velocity zone, *Tectonophysics*, *416*, 53–79.

Turcotte, D. L., and J. Phipps Morgan (1992), The physics of magma migration and mantle flow beneath a mid-ocean ridge, in *Mantle Flow and Melt Generation at Mid-Ocean Ridges*, *Geophys. Monogr. Ser.*, vol. 71, edited by J. Phipps Morgan, D. K. Blackman, and J. M. Sinton, pp. 155–182, AGU, Washington, D. C.

Turcotte, D. L., and G. Schubert (1982), *Geodynamics: Applications of Continuum Physics to Geological Problems*, John Wiley, New York.

Walter, M. J. (1998), Melting of garnet peridotite and the origin of komatiite and depleted lithosphere, *J. Petrol.*, *39*, 29–60.

Watts, A. B. (2001), *Isostasy and Flexure of the Lithosphere*, Cambridge Univ. Press, Cambridge, U. K.

Webb, S., and B. J. Wood (1986), Spinel-pyroxene-garnet relationships and their dependence on Cr/Al ratio, *Contrib. Mineral. Petrol.*, *92*, 471–480.

Wood, B. J., and D. A. Yuen (1983), The role of lithospheric phase transitions on seafloor flattening at old ages, *Earth Planet. Sci. Lett.*, *66*, 303–314.

Yang, Y., D. Forsyth, and D. Weeraratne (2007), Seismic attenuation near the East Pacific Rise and the origin of the low-velocity zone, *Earth Planet. Sci. Lett.*, *258*, 260–268.

Yliniemia, J., E. Kozlovskayaa, S. Hjeltb, K. Komminahob, and A. Ushakov (2004), Structure of the crust and uppermost mantle beneath southern Finland revealed by analysis of local events registered by the SVEKALAPKO seismic array, *Tectonophysics*, *394*, 41–67.

Zaranek, S. E., and E. M. Parmentier (2004), The onset of convection in fluids with strongly temperature-dependent viscosity cooled from above with implications for planetary lithospheres, *Earth Planet. Sci. Lett.*, *224*, 371–386.

Zeyen, H., and M. Fernàndez (1994), Integrated lithospheric modeling Combining thermal, gravity, and local isostasy analysis: Application to the NE Spanish Geotransect, *J. Geophys. Res.*, *99*, 18,089–18,102.

Zeyen, H., P. Ayarza, M. Fernàndez, and A. Rimi (2005), Lithospheric structure under the western African-European plate boundary: A transect across the Atlas Mountains and the Gulf of Cadiz, *Tectonics*, *24*, TC2001, doi:10.1029/2004TC001639.

Zhao, L. S., and D. V. Helmberger (1993), Upper-mantle compressional velocity structure beneath the northwest Atlantic Ocean, *J. Geophys. Res.*, *98*, 14,185–14,196.

Zhao, M., C. Langston, A. Nyblade, and T. Owens (1999), Upper mantle velocity structure beneath southern Africa from modeling regional seismic data, *J. Geophys. Res.*, *104*, 4783–4794.

Zhao, Y., R. B. Von Dreele, T. J. Shankland, D. J. Weidner, J. Zhang, Y. Wang, and T. Gasparik (1997), Thermoelastic equation of state of jadeite $NaAlSi_2O_6$: An energy-dispersive Reitveld refinement study of low symmetry and multiple phases diffraction, *Geophys. Res. Lett.*, *24*, 5–8.

Zheng, J., W. L. Griffin, S. Y. O'Reilly, M. Zhang, N. J. Pearson, and Z. Luo (2006), The lithospheric mantle beneath the southern Tianshan area, NW China, *Contrib. Mineral. Petrol.*, *151*, 457–479.

Zienkiewicz, O. C. (1977), *The Finite Element Method*, McGraw-Hill, New York.